TAMPEREEN TEKNILLINEN YLIOPISTO
TAMPERE UNIVERSITY OF TECHNOLOGY

LAURI HYTÖNEN

HEAT MANAGEMENT IN HIGH-EFFICIENCY PHOTOVOLTAICS

Master of Science thesis

Examiners: D.Sc. Ville Polojärvi and D.Sc. Arto Aho
Examiner and topic approved by the Dean of the Faculty of Natural Sciences on 30th of May 2018

ABSTRACT

LAURI HYTÖNEN: Heat management in high-efficiency photovoltaics
Tampere University of Technology
Master of Science thesis, 72 pages
June 2018
Master's Degree Programme in Science and Engineering
Major: Advanced Engineering Physics
Examiners: D.Sc. Ville Polojärvi and D.Sc. Arto Aho
Keywords: heat management, high-efficiency, multi-junction solar cell, concentrated photovoltaics, COMSOL, III–V semiconductors

Multi-junction solar cells are one of the most promising technologies for solar energy production in both terrestrial and space applications. Highest conversion efficiencies among all solar cells have been recorded by III–V multi-junction solar cells under concentrated sunlight. Concentration of light improves the overall efficiency of the solar cell, but also increases the heat load, which has negative impact on the cell performance. In order for concentrated photovoltaics to remain as a competitive alternative for solar energy production, adequate heat management must be implemented.

In this thesis, a thermal simulation model for concentrated photovoltaics is developed. The key aspect of the model is the incorporation of concentration and temperature dependency of efficiency of the simulated multi-junction solar cell. By defining the temperature dependency of the efficiency, we can study the impact of the temperature on the performance of a single cell and the overall performance of a panel assembly. The model is validated by comparing data acquired from laboratory measurements with data acquired from the simulation. The model is then extended to study different cooling scenarios.

Five different scenarios were investigated on a panel level: passive cooling, active cooling, cell miniaturisation, concentrated photovoltaics in space conditions and sub-bandgap energy photon filtering. The model proved to be a useful tool in predicting the behaviour of different cooling scenarios. The results were predictable and in agreement with the theory. The model offers valuable insight to different cooling scenarios by providing numerical information about the power output at single cell and panel scale. This information could be used e.g. for evaluating the payback period of the capital invested in the cooling system. The model presented in this thesis can easily be extended to study different scenarios by either varying existing parameters or by adding new parameters or boundary conditions.

TIIVISTELMÄ

LAURI HYTÖNEN: Lämmön hallinta korkean hyötysuhteen aurinkokennoissa
Tampereen teknillinen yliopisto
Diplomityö, 72 sivua
Kesäkuu 2018
Teknis- luonnontieteellinen koulutusohjelma
Pääaine: Teknillinen fysiikka
Tarkastajat: TkT Ville Polojärvi ja TkT Arto Aho
Avainsanat: lämmönhallinta, korkea hyötysuhde, moniliitosaurinkokenno, keskitetyn valon aurinkosähkö, COMSOL, III–V puolijohteet

Moniliitosaurinkokennot ovat yksi lupaavimmista teknologioista aurinkoenergian tuottamiseksi sekä maanpäällisissä olosuhteissa että avaruudessa. Aurinkokennojen suurimmat hyötysuhteet on saavutettu III–V puolijohteista valmistetuilla moniliitosaurinkokennoilla keskitetyn auringonvalon alla. Valon keskittäminen parantaa kennon hyötysuhdetta, mutta kasvattaa samalla kennoon kohdistuvaa lämpökuormaa, joka puolestaan vaikuttaa negatiivisesti kennon suorituskykyyn. Jotta kohdennetun valon aurinkokennot pysyisivät kilpailukykyisenä vaihtoehtona aurinkoenergian tuottamisessa, on jäähdytyksen oltava riittävä.

Tässä diplomityössä kehitetään kohdennetun valon aurinkokennojen lämmön mallintamiseen soveltuva simulaatiomalli. Mallin tärkein ominaisuus on mallinnetun kennon hyötysuhteen lämpötila- ja konsentraatioriippuvuuden huomioiminen. Määrittelemällä kennon hyötysuhteen lämpötilariippuvuus malliin, voidaan tarkastella, millainen vaikutus lämpötilalla on yksittäisen kennon ja koko paneelin toimintaan. Mallin toimivuus vahvistetaan vertailemalla siitä saatuja tuloksia laboratoriossa tehtyjen mittausten kanssa. Tämän jälkeen mallia laajennetaan erilaisiin jäähdytystilanteisiin.

Viittä erilaista tilannetta mallinnettiin paneelitasolla: passiivista jäähdytystä, aktiivista jäähdytystä, kennon koon pienentämistä, kohdennetun valon aurinkopaneeleita avaruusolosuhteissa sekä energialtaan energia-aukon energiaa alhaisempien fotonien suodatusta. Simulaatiomalli osoittautui hyödylliseksi työkaluksi erilaisten jäähdytystilanteiden mallintamiseksi. Tulokset olivat ennustettavissa ja yhtenevät teorian kanssa. Malli tarjoaa syventävää, numeerista näkemystä yksittäisen kennon ja kokonaisen paneelin energiantuottoon. Tätä tietoa voitaisiin hyödyntää esimerkiksi jäähdytykseen investoidun pääoman takaisinmaksuajan arvioinnissa. Työssä kehitettyä simulaatiomallia pystyy helposti laajentamaan joko muuttamalla olemassa olevia parametreja tai lisäämällä uusia parametreja tai reunaehtoja.

PREFACE

The work presented in this thesis was conducted at the Optoelectronics Research Centre (ORC) of Laboratory of Photonics, Tampere University of Technology. The work was financially supported by the Fortum Foundation, Tekes project BrigthSky and ERC project Ametist. I would like to express my gratitude to the head of ORC, Prof. Mircea Guina. Thank you for giving me the initial chance to work with my B.Sc. thesis three years ago and for letting me continue working in the solar cell team. I highly value the experience I got.

I would like to thank the examiners and instructors of this thesis, Dr. Ville Polojärvi and Dr. Arto Aho for guiding me with this work. Special thanks goes to Ville for being my supervisor since my first day at ORC and for always encouraging me to explore my own ideas. I also want to thank Arto for ideas and great discussions related to simulations, processing and measurements during the past three years. This thesis is a concrete result of an idea that initially started from one of our discussions.

I would like to acknowledge the rest of the solar cell team: Dr. Antti Tukiainen, M.Sc. Timo Aho, M.Sc. Marianna Raappana, M.Sc. Riku Isoaho and M.Sc. Jarno Reuna. I have learned a lot about solar cells and semiconductors from you. Special thanks go to Timo and Marianna for being my office mates—we've had good laughs during the past years. I also want to thank the supportive staff of ORC as well as all the kind people that made working at ORC enjoyable and memorable.

Finally, I would like to thank my family and friends for their continuous support. Especially I want to thank Henni for withstanding my long days with my studies and for endless support.

Tampere, May 22nd, 2018

Lauri Hytönen

CONTENTS

LIST OF FIGURES

LIST OF TABLES

LIST OF ABBREVIATIONS AND SYMBOLS

AM	air mass
BOS	balance of system
CMYC	Cooper-Mikic-Yovanovich correlation
CPV	concentrated photovoltaics
CPVT	concentrated photovoltaic thermal
c-Si	crystalline silicon
DBC	direct bonded copper
DNI	direct normal irradiance
FEM	finite element method
FF	fill factor
IV	current-voltage
LM	least-material
MBE	molecular beam epitaxy
MOCVD	metal-organic chemical vapour deposition
PMMA	polymethyl methacrylate
PV	photovoltaics

α	material dependent parameter in Varshni relation
β	material dependent parameter in Varshni relation
γ	recombination dependent parameter
ϵ	emissivity
η	efficiency
θ	inclination angle
μ	dynamic viscosity
ν	kinematic viscosity
λ	wavelength
ρ	density
σ	Stefan-Boltzmann constant
ϕ	coefficient of volume expansion of a fluid
ψ	basis function

A	area
c	speed of light
C_p	heat capacity
D	thermal diffusivity

e	Euler's number
E	emission power of a black body
E_c	conduction band energy
E_f	Fermi level
E_g	band gap energy
$E_{g,0}$	band gap energy at 0 K
E_v	valence band energy
g	gravitational acceleration
Gr	Grashof number
h	Planck constant
H	convective heat transfer coefficient
I	current
I_0	dark saturation current
I_{mp}	current at maximum power point
I_{op}	optically generated current
I_{sc}	short circuit current
I_{sun}	intensity of the sun
k	coefficient of thermal conductivity
k_B	Boltzmann constant
n_{opt}	optical efficiency
Nu	Nusselt number
Pr	Prandtl number
P_{mp}	power at maximum power point
q	elementary charge
Q	heat transfer rate
$\overrightarrow{Q}$	local heat flux density
Ra	Rayleigh number
Re	Reynolds number
R_s	series resistance
T	temperature
u	variable in a partial differential equation
u_h	approximation function for u
v_∞	velocity outside boundary layer
V	voltage
V_{mp}	voltage at maximum power point
V_{oc}	open circuit voltage
V_{ocd}	direct open circuit voltage
X	concentration factor

1. INTRODUCTION

While the global energy consumption continuously increases, the aim towards lower carbon dioxide (CO_2) emissions drives the market to create more efficient ways to produce renewable energy. Although most of the renewable energy in 2016 was produced by wind power, solar energy is catching up fast: In 2015 the production capacity of solar energy rose by 32.6%, recording the largest growth increment to date [11]. In 2016, solar photovoltaics (PV) represented 47% of newly installed renewable power capacity [40]. Polycrystalline silicon solar cells have dominated the solar industry since the beginning. However, technologies such as perovskite solar cells and multi-junction solar cells keep improving their efficiency making them viable competitors [1].

Highest conversion efficiencies have been recorded by III–V semiconductor multi-junction solar cells. In multi-junction architecture the solar spectrum is split between subcells. Each subcell is capable of converting different parts of the spectrum into electricity. This approach reduces thermalisation losses, resulting in higher conversion efficiencies. Multi-junction solar cells are the best choice for concentrator applications. In concentrated photovoltaic (CPV) systems sunlight is concentrated to the cell by optical components, such as lenses or mirrors. This has two major benefits: First of all, less cell material is needed for covering the same area as without concentrator. Secondly, the conversion efficiency can improve significantly under concentration. The best conversion efficiencies has been recorded by CPV multi-junction cells. Current world record holder is a 4-junction GaInP/GaAs/GaInAsP/-GaInAs cell operating under concentration of 508 suns at a conversion efficiency of 46.0% [24]. In addition to CPV, III–V multi-junction solar cells are also excellent choice for extraterrestrial applications due to their high power-to-mass-ratio and irradiation hardness.

However, concentrating sunlight to a small spot greatly increases the heat load of the cell, which has negative effects on the power output of the cell. As the operating temperature of the cell increases, two phenomena can be observed: the current is slightly increased but the voltage of the cell decreases. However, the gain in current can not compensate the loss in the voltage, which results in the loss of efficiency.

This effect is even greater with silicon solar cells due to their low operating voltage compared to III–V semiconductor solar cells. To keep the solar cell working at maximum efficiency, heat must be transferred away from the cell. In traditional CPV panels the heat is absorbed by a heatsink, which then emits the heat away or transfers it to the surrounding air. Therefore, with current conversion efficiencies over 50% of the input energy is lost as heat. However, in concentrated photovoltaic thermal collector (CPVT) systems the thermal energy produced by the cell is also collected. These hybrid systems have already achieved system efficiencies as high as 65.1% [41].

In 2016 a flat-plate crystalline silicon (c-Si) system cost 1.0 €/W, which can be further broken down into 0.55 €/W for modules, 0.11 €/W for inverters and 0.34 €/W for balance of system (BOS) costs. Projected cost of the c-Si system in 2020 is 0.75 €/W. In order to compete with this, a CPV system has to achieve a 40% system efficiency. This suggests a module efficiency of 44% and cell efficiency of 50% under 1000-sun concentration. [18] The required operating efficiencies cannot be achieved without adequate heat management.

In this thesis, the general requirements for heat management in CPV systems are studied. This is achieved by establishing a thermal model of a CPV system, which is first verified with laboratory measurements. Then the model is further extended to find general guidelines for cooling provided by different scenarios. The temperature dependency of the efficiency of the solar cell is coupled with the thermal model and therefore has an effect on the amount of heat generated in the cell. Although the cooling requirements are presented from the perspective of a concentrated III–V multi-junction solar cell system, the principles and models described in this thesis could be applied to other solar cell types with some adjustments. The work was conducted at Optoelectronics Research Centre, Tampere University of Technology.

This thesis consists of 7 chapters in total. In Chapter 2, the basics of semiconductors, semiconductor solar cells and concentrated photovoltaics are presented. In addition, the focus is in describing how the operating temperature affects the performance of the cell. In Chapter 3 the basics of heat transfer mechanisms are discussed, as they all take a role in cooling down a solar cell. Chapter 4 addresses the research methods used in this thesis, which consist of two main parts: laboratory measurements and simulations. Here we establish the constraints, geometries and boundary conditions used in the simulation model. Chapter 5 includes various studies of cooling schemes for CPV. In Chapter 6 the simulation results are analysed and compared to literature. Finally, the work is concluded in Chapter 7.

2. SEMICONDUCTOR SOLAR CELLS

Solar cells are devices that convert sunlight into electricity i.e. photons into electrons. The mechanism behind this conversion varies between solar cell types. In this thesis the theory is presented from the point of view of III–V semiconductors. It is important to understand the basic operating principles of solar cells to justify why heat management in solar cell applications is important. This chapter covers the physical background of semiconductor solar cells, multi-junction solar cells and concentrated photovoltaics.

2.1 Semiconductors

In general, materials are divided into three categories based on their ability to conduct electricity; conductors, insulators and semiconductors. Metals are an example of conductive materials; they have a lot of free electrons to conduct electricity. However, metals are usually opaque, and light cannot travel inside them thus making them poor materials for optoelectronic devices. In contrast, insulators, such as glass and other dielectric materials, are usually highly transparent, but do not conduct electricity. Semiconductors are materials that have electrical conductivities between conductors and insulators while being semi-transparent. Elemental semiconductors are generally found in column IV in the periodic table of elements. In addition, compound semiconductor materials can be manufactured by combining elements from groups III and V as well as from groups II and VI. [37] Most common methods for manufacturing compound semiconductor materials are metal-organic chemical vapour deposition (MOCVD) and molecular beam epitaxy (MBE).

To understand the electrical properties of a semiconductor, we must first understand the band structure. Electrons in a single isolated atom occupy discrete energy levels called atomic orbitals. As stated by Pauli exclusion principle, no two fermions can occupy the same quantum state within a quantum system. So, two identical atoms can have identical electronic structures when they are not interacting with each other. However, as these two isolated atoms are brought together, it is apparent that their wave functions start to interact and overlap. As they cannot occupy the

same quantum state any more, the discrete energy levels start to split. When many atoms are brought together in a solid, these split energy levels start to form energy bands of allowed states. The energy band occupied by the outermost electrons, valence electrons, is called the valence band and the band above it is called the conduction band. The energy difference between these two bands is called the band gap E_g, which is usually measured in electron volts. At 0 K all the valence electrons are located in the valence band. When the temperature rises, some of the valence electrons are promoted to the conduction band via thermal excitation, leaving behind an unoccupied state in the valence band. These electrons in the conduction band are no longer tied to the crystalline structure and they are free to conduct electricity. The unoccupied states in the valence band are called holes. Each semiconductor material has its own unique band structure and consequentially unique band gap energy. [22, 44]

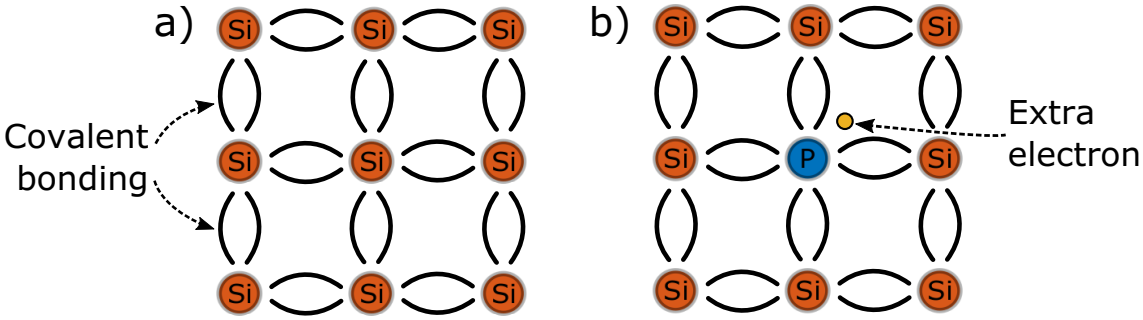

Figure 2.1 *Covalent bonding in silicon. a) Silicon forms covalent bonds with neighbouring atoms by sharing the electrons. b) When a silicon atom is replaced with phosphorus atom, one electron is not contributing to the covalent bonding.*

The electrical conductivity of a semiconductor material can be varied over orders of magnitude with material choices, excitation and impurity doping. Consider a silicon atom; silicon has four valence electrons, two in the 2s orbital and two in the 2p orbital. In a crystalline structure silicon forms covalent bonds by sharing its valence electrons with the neighbouring atoms, as seen in Figure 2.1a. If a silicon atom were replaced with an atom from group V (eg. phosphorus), there would be one electron that does not contribute to the covalent bonding (Figure 2.1b). This excess electron has an energy level considerably higher than those in the valence band, thus being easier to promote to the conduction band. For group IV elements, dopants from group V are called donors and dopants from group III are called acceptors. A semiconductor doped with donors is called an n-type semiconductor, since they introduce free electrons (negative charge carriers) to the structure. Similarly a semiconductor doped with acceptors is called p-type semiconductor, since they introduce holes (positive charge carriers) to the structure. By changing the doping concentrations in the semiconductor, the electrical properties can be tailored.

2.2 Basic operating principles of solar cells

The operation of semiconductor solar cells is based on the photovoltaic effect, in which electromagnetic radiation interacts with matter. When a photon with energy greater than the band gap energy E_g interacts with an electron in the valence band, the energy is absorbed by the electron. An electron-hole-pair is created; the electron rises to the conduction band, leaving a hole to the valence band. As the electrons in the conduction band are not tied to the crystalline structure, they are "free" to move thus being able to conduct electrical current. However, if the charge carriers, electrons and holes, are not separated, they will eventually recombine. To prevent recombination and eventually the loss of energy, an intrinsic electric potential is created with a pn-junction.

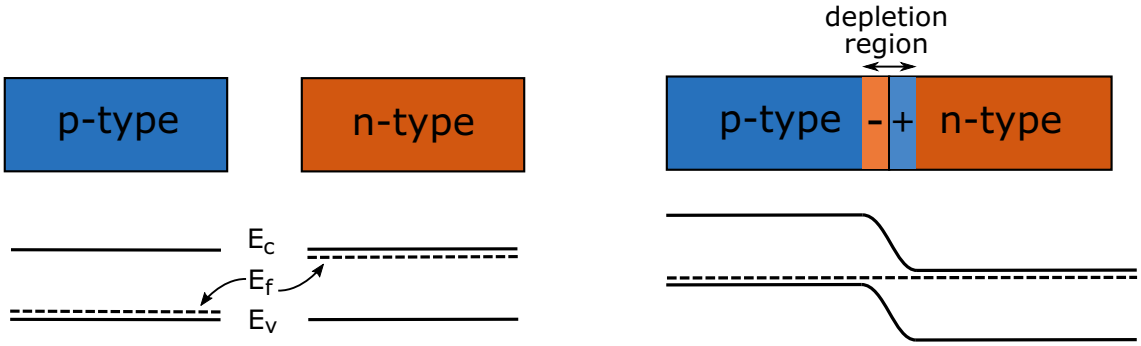

Figure 2.2 *Formation of a pn-junction. On the right the valence band (E_v) and the conduction band (E_c) have bent so that the Fermi level (E_f) of both materials align.*

In a pn-junction p-type and n-type semiconductor materials are brought together. Since there is a concentration difference of electrons and holes in the structure, holes start to diffuse into the n-type semiconductor and the electrons diffuse into the p-type semiconductor. Initially the n- and p-type semiconductor materials were electrically neutral, but the diffusion of electrons and holes result in positively and negatively charged regions. This creates an electrostatic potential difference across the junction (Figure 2.2), which limits the diffusion further. This region between the two types of semiconductors is called the depletion region, because it is essentially depleted from free charge carriers. In thermal equilibrium the net current and voltage over the junction are zero.

The thermal equilibrium can be disturbed with external voltage applied across the junction. Let's define the applied voltage V to be positive when the external bias is positive on the p side of the junction. When biased positively, the electrostatic barrier of the junction is lowered and the depletion region narrows down. This increases the drift current across the junction and as a consequence a positive net

current flows through the device, as seen in Figure 2.3. This configuration is called forward bias. In contrast, when the junction is in reverse bias the depletion region widens and the diffusion current is reduced. However, even though the depletion region is very wide, some thermally generated charge carriers reach the junction due to diffusion and are swept across the junction resulting in a small negative current. In small reverse bias voltages there is a small increase in the negative current. This current saturates when the reverse bias is further increased, as is seen in the Figure 2.3. This current is called the reverse saturation current or dark saturation current [51]. The current flowing through a pn-junction when external voltage bias is applied can be expressed with the diode equation

$$I = I_0(e^{qV/nk_BT} - 1), \tag{2.1}$$

where I_0 is the dark saturation current, q is the elementary charge, V is the applied voltage, n is the ideality factor, k_B is the Boltzmann constant and T is the temperature of the junction. The ideality factor n has usually values between one and two. It is used to describe the non-idealities of actual pn-junctions.

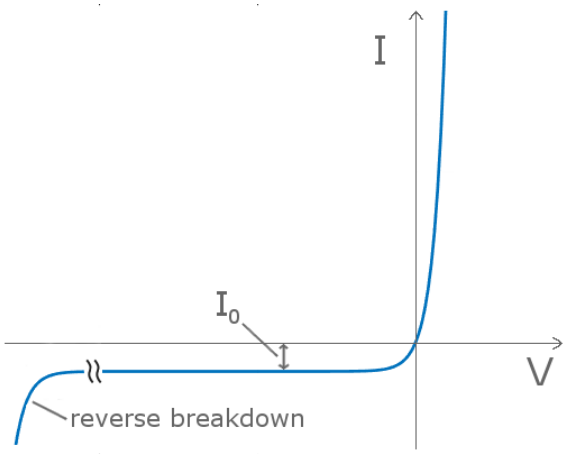

Figure 2.3 *Current-voltage-characteristics of a pn-junction in reverse and forward bias.*

When illuminated, photons with energy $E \geq E_g$ are absorbed in the pn-junction. The absorbed photons create electron-hole pairs, resulting in free charge carriers. It is important to note, that even though absorption happens at every depth of the semiconductor material, only the electron-hole pairs within the depletion region are automatically separated by the internal electric field. Electron-hole pairs that are located within the diffusion length from the depletion region are also likely to reach the depletion region and contribute to the generated current. Rest of the generated electron-hole pairs will eventually recombine, and their energy is released to the crystal as phonons (i.e. heat). The drift of the carriers across the depletion region

weakens the innate electric field. This appearance of a forward voltage is known as the photovoltaic effect [44, p. 400]. To model the pn-junction under illumination, the optically generated current is subtracted from the diode equation 2.1, resulting in

$$I = I_0(e^{qV/nk_BT} - 1) - I_{op}, \tag{2.2}$$

where I_{op} is the optically generated current. This shifts the current-voltage (IV) -curve of the diode down in y-axis, and the resulting curve is a superposition of the dark-IV-curve and the generated current. Because the junction is generating current under illumination, the y-axis of the plot is usually flipped, as seen in figure 2.4.

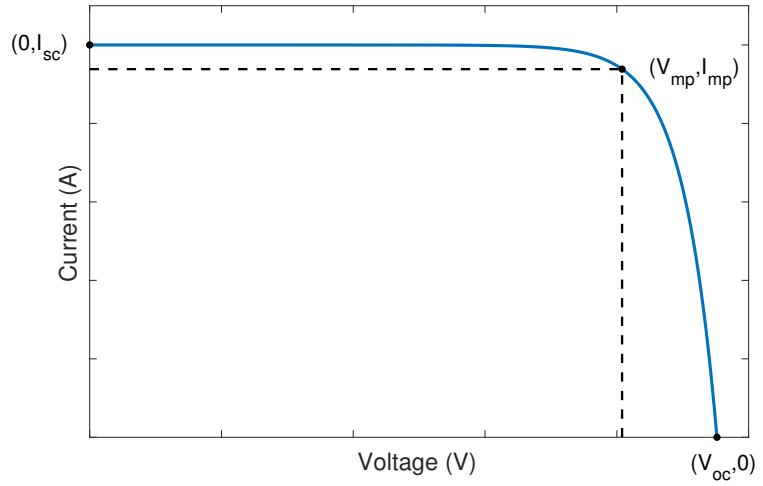

Figure 2.4 *IV-characteristics of a pn-junction under illumination.*

Figure 2.4 is a good illustration of several important figures of merit of solar cells. The current at zero voltage, i.e. when the cell is short-circuited, is called the short circuit current, denoted with I_{sc}. Ideally, this is equal to the photogenerated current [22], thus being directly proportional to the intensity of incoming light. The second parameter is the open circuit voltage V_{oc}. Setting I to zero in equation 2.2 and rearranging results in

$$V_{oc} = \frac{nk_BT}{q} ln\left(\frac{I_{op}}{I_0} + 1\right). \tag{2.3}$$

This could be interpreted so, that the V_{oc} of the cell is determined by the properties of the semiconductor, which affect the value of I_0 [22]. When $I_{op} \gg I_0$, Equation 2.3 is often approximated by

$$V_{oc} \approx \frac{nk_BT}{q} ln\left(\frac{I_{op}}{I_0}\right), \tag{2.4}$$

as shown by [31, p. 112]. In addition, as the output power of the cell is the product of current and voltage, at the knee point of the curve the cell reaches its maximum operating efficiency. This point is called the maximum power point (P_{mp}), which is defined as

$$P_{mp} = V_{mp}I_{mp}, \tag{2.5}$$

where V_{mp} and I_{mp} are the voltage at maximum power point and the current at maximum power point, respectively. One additional feature that can be extracted from the IV-curve is the fill factor (FF), which measures the "squareness" of the IV-plot. It is defined as

$$FF = \frac{V_{mp}I_{mp}}{V_{oc}I_{sc}} = \frac{P_{mp}}{V_{oc}I_{sc}}. \tag{2.6}$$

This could be interpreted graphically as the ratio of rectangular areas defined by V_{mp}, I_{mp}, V_{oc} and I_{sc}. In essence FF describes the quality of the cell. The closer the FF is to one, the better the cell. In addition, one of the most commonly used figure of merit of solar cells is the conversion efficiency. The efficiency is defined as the ratio of the maximum produced power and input power, i.e.

$$\eta = \frac{P_{mp}}{P_{in}} = \frac{FF\,V_{oc}I_{sc}}{P_{in}} \tag{2.7}$$

In order to maximise the efficiency of the cell, the FF, V_{oc} and I_{sc} need to be maximised.

2.3 Multi-junction solar cells

The Sun produces energy by nuclear fusion and emits energy as photons to its surroundings. The energy of the emitted photons is broad ranging from almost 0 to 4 eVs [31, p. 319], and the spectrum follows very closely the spectrum emitted by a black body at 5772 K. The intensity of solar irradiation outside Earth's atmosphere is 1366.1 W/m^2 based on the ASTM E-490 standard [34]. This is usually referred as the AM0 spectrum, as there is no (zero) air mass (AM) between the sun and

the irradiation surface. However, as the light passes through Earth's atmosphere, the chemical compounds (such as water vapor and CO_2) absorb and scatter the light. The longer the optical path in the atmosphere, the bigger the air mass and thus more irradiation is absorbed or scattered. This alters the spectrum of the sun at Earth's ground level. AM1.0 would be the thickness of the atmosphere around the Earth. AM1.5 is reached at 37° tilt from normal, which is commonly used in characterisation of terrestrial solar cells. The ASTM G173-03 standard defines the integrated intensities of AM1.5D and AM1.5G spectra to be 900.1393 W/m^2 and 1000.3707 W/m^2, respectively [33]. The mentioned spectra are presented in Figure 2.5.

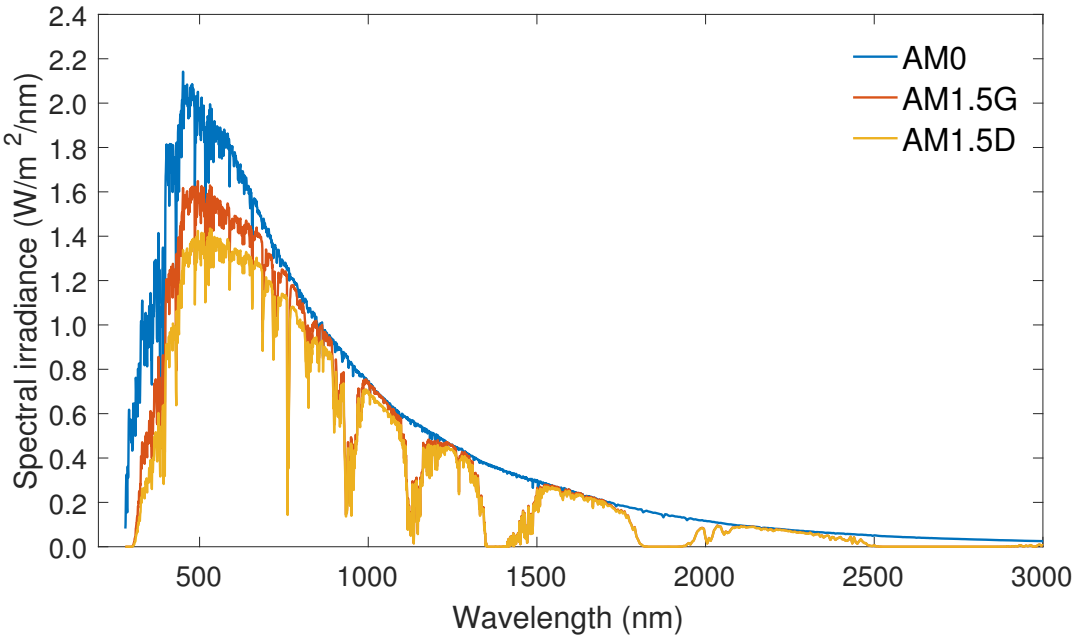

Figure 2.5 *The Sun's spectra with different air masses. Data is taken from [33].*

The AM1.5G spectrum includes both direct and diffuse sunlight, thus having slightly higher intensity than the AM1.5D spectrum, which in contrary includes only direct sunlight that has passed through the atmosphere. The AM1.5D spectrum is usually used in characterisation of CPV solar cells, as the concentrators mainly gather direct sunlight and only small part of the diffuse sunlight. The absorption of different compounds is clearly visible in the sun's spectrum, and there are several spectral gaps with almost no irradiation. Also, both UV and visible light are slightly absorbed in AM1.5 compared to AM0.

Let's consider a solar cell with a bandgap of E_g. As mentioned in Section 2.2, only photons with energy $hf \geq E_g$ are capable of promoting the electron from conduction band to valence band. This means, that all photons with energy below the band gap are lost as heat. In addition, for every photon with energy above the band

gap the energy difference $hf - E_g$ is lost as heat. Thus, a solar cell consisting of a single semiconductor material cannot achieve high conversion efficiencies. In fact, the detailed balance limit of a single-junction solar cell operating at 300 K is around 31% [42]. To tackle this problem, a rather simple solution exists: by splitting the spectrum into several spectral regions and by matching their respective energies with semiconductor materials with different bandgaps, higher conversion efficiencies can be reached. A solar cell consisting of several different semiconductor materials with different bandgaps stacked on top of each other is called a multi-junction solar cell. The stacking can be done e.g. by monolithic growth or wafer bonding. The spectral splitting in a multi-junction solar cell is illustrated in Figure 2.6. In III–V multi-junction solar cells the cells must be stacked so that $E_{g\,top} > E_{g\,middle} > E_{g\,bottom}$ for successful spectral splitting. Otherwise the subcells with lower bandgaps would absorb light from other cells.

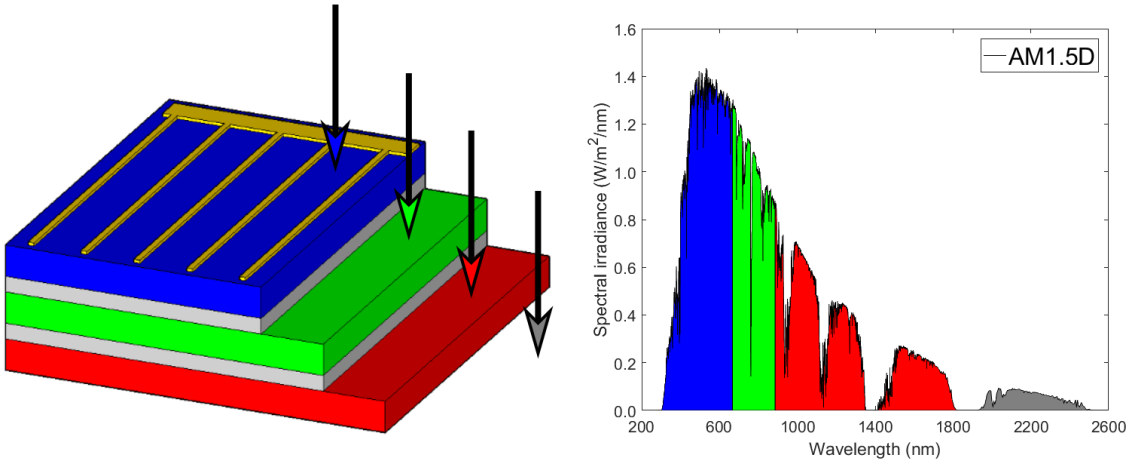

Figure 2.6 *Spectral splitting in a III–V multi-junction solar cell. The stacked cells absorb different parts of the spectrum according to their bandgaps. Photons with energy lower than the bandgap pass through to lower subcells. Photons below the lowest bandgap (marked in grey) are either reflected away or lost as heat.*

The subcells of a monolithic III–V multi-junction solar cell are electrically connected in series. However, if the cells were just stacked on top of each other, there would be p- and n-type semiconductor interfaces connected to each other creating new pn-junctions at the subcell interfaces. These would roughly negate the photovoltage generated by subcells. To overcome this, a tunnel-junction interconnect is usually grown between the subcells. A tunnel-junction is a very thin, highly doped pn-junction, which provides a low resistance connection between the subcells. High doping of the tunnel-junction creates a very narrow depletion region, which allows electrons to tunnel from n-side to p-side even at low voltages. In addition to low resistance, tunnel-junctions must be highly transparent to the light transmitted by the cells above. [31, pp. 349–350]

Each subcell in a multi-junction architecture obeys the operating principles described in Section 2.2. However, to model the operation of a multi-junction solar cell, the electrical connection between subcells must be taken into account. First of all, the voltage of the multi-junction cell is given by the sum of individual subcells, i.e.

$$V_{tot} \approx \sum_{i=i}^{m} V_i, \qquad i = 1, 2, 3, ..., m\,, \tag{2.8}$$

where V_i is the voltage of the ith subcell and m is the number of subcells [31, p. 324]. Secondly, the current flowing through the cells must be the same for each subcell, thus being limited by the subcell with lowest current generation, i.e.

$$I_{mj} = min(I_i), \qquad i = 1, 2, 3, ..., m, \tag{2.9}$$

where I_i is the current produced by the ith subcell. Ideally, multi-junction solar cells are designed to be current matched i.e. each cell outputs the same current. This can be done e.g. by selecting the bandgaps of the subcells adequately, or by adjusting the absorption of each subcell. Because the absorption coefficient of each subcell is finite, some above-bandgap light is always passed through to the lower level cells. Thus, the current generated by each subcell can be tuned by changing the thickness of the cells. For example, more light can be passed to lower bandgap cells by thinning the top cell. However, due to sensitivity to temperature and spectrum, exact current matching between subcells is rarely achieved. Now the IV-behaviour of the multi-junction solar cell under illumination is given by

$$V_i = \frac{nk_BT}{q}\, ln(1 + \frac{I_{op,i} - I_{mj}}{I_{0,i}}) - I_{mj}R_{s,i} \qquad i = 1, 2, 3, ..., m\,. \tag{2.10}$$

As the operating current of the multi-junction solar cell is the current of the limiting subcell, the cell is able to operate at the maximum power point only if all subcells operate at their respective maximum power points. As the current is rarely perfectly matched between subcells, some of the subcells will always be operating away from their maximum power point.

2.4 Concentrated photovoltaics

In concentrated photovoltaics, light is gathered from a large area to a cell with optical elements such as lenses or mirrors. This offers two major advantages. Firstly, fewer

solar cells are needed to cover the same area as with solar cells operating at one sun. This translates directly to lower production costs, as less cell material is required. Secondly, the efficiency of the solar cell is improved, which reduces the payback time of the system. If sunlight is concentrated by a factor of X on a cell with a short-circuit current of I_{sc}, the short-circuit current for the concentrated cell is

$$I_{sc}^{X} = X \cdot I_{sc} \tag{2.11}$$

Substituting Equation 2.11 to Equation 2.4 yields

$$V_{oc}^{X} \approx \frac{nk_BT}{q} ln\left(\frac{XI_{sc}}{I_0}\right) \tag{2.12}$$

$$V_{oc}^{X} \approx \frac{nk_BT}{q} \left[ln\left(\frac{I_{sc}}{I_0}\right) + ln\, X\right] \tag{2.13}$$

$$V_{oc}^{X} \approx V_{oc} + \frac{nk_BT}{q} ln\, X. \tag{2.14}$$

From Equation 2.14 it can be seen that the open circuit voltage of the cell rises as a function of the concentration. Combined with Equation 2.7, we get

$$\eta = \frac{FF^X\, V_{oc}^X\, XI_{sc}}{X\, P_{in}} = \frac{FF^X\, V_{oc}^X\, I_{sc}}{P_{in}}. \tag{2.15}$$

At low concentrations we can assume that $FF^X \approx FF$, thus the efficiency of the cell increases with increased illumination. However, FF is not totally independent of the concentration. At 400-1000 suns concentration it starts to decrease [2], ultimately limiting the maximum output power of the solar cell.

In general, there are two approaches for concentrating sunlight onto a solar cell. Firstly, refractive optics such as Fresnel lenses are commonly used. A Fresnel lens is a plano-convex lens which has been collapsed at several loctions to make it thinner and lighter. Usually they are made from Acrylic plastic or polymethyl methacrylate (PMMA). These lenses can be point-focus i.e. circularly symmetrical or linear focus, which focus light on a line. Alternatively, reflective optics such as paraboloid mirros are also used. A paraboloid shaped surface has a single focal point for all reflected rays that are parallel to the axis of the parabola. [31, pp. 452–454]. With Fresnel

lenses concentrations up to 1000 suns are achievable. Concentrations beyond this are limited by chromatic aberration [36, p. 97] and cannot be achieved without secondary optics. With linear parabolic reflectors only concentrations ranging from 70 to 200 can be achieved reliably without secondary optics [36, p. 99].

Concentrating sunlight from a big area to a small cell brings also a few downsides. First of all, the heat load of the solar cell is increased greatly. This has negative effects on the operating efficiency of the cell, which will be discussed more detailed in Section 2.5. In addition, for the concentrating optics to work as designed, the cell and the concentrating optics need to be aligned precisely with the sun. This requires precise tracking of the sun as well as precise assembly of the panel, increasing the manufacturing, installation and maintenance costs. However, during the course of day, tracking also increases the energy output of the panel: Consider conventional silicon solar panels that are installed at a static angle. Their maximum area is irradiated only when the installation angle is equal to the sun's angle. At the beginning and at the end of the day, when the sun shines at low angles, most of the irradiation is wasted. This is also usually the time when the need for electricity is at its highest. In CPV and other tracking systems tracking the sun means that the cell and the optics are always aligned so that they are facing directly at the sun, producing power more efficiently—even at low angles.

2.5 Influence of temperature on solar cell performance

Like all semiconductor devices, also semiconductor solar cells are sensitive to temperature. In typical operation conditions the cell parameters vary linearly with temperature. From Equation 2.6 we can deduce a formula for maximum output power. The temperature dependency of maximum output power can be expressed as a function of the temperature dependencies of the individual factors, i.e.

$$P_{mp}(T) = V_{oc}(T)\, I_{sc}(T)\, FF(T). \tag{2.16}$$

The temperature dependency of the V_{oc} accounts for 80-90% of the temperature coefficient of efficiency [23]. The open-circuit configuration of the cell corresponds to the state where the photogenerated current is equal to the recombination. Thus, the temperature dependency of V_{oc} is in essence the temperature dependency of the photogeneration-recombination balance [17]. Despite the linear dependency on T in Equation 2.4, the V_{oc} is highly dependent on the logarithmic ratio of I_{op} and I_0. The dark saturation current I_0 has strong dependency on temperature due to

quasi-Fermi statistics, which we will not deal in detail here. The derivation of the temperature dependency of V_{oc} is well presented by Dupré et. al. in [17, pp. 46–50], and the result is found to be

$$\frac{dV_{oc}}{dT} = \frac{\frac{E_{g0}}{q} - V_{oc} + \gamma\frac{kT}{q}}{T}, \tag{2.17}$$

where E_{g0} is the band gap at 0 K and coefficient γ is dependent on the recombination method. In case of Shockley-Read-Hall recombination, where the transitioning electron from a band to another is trapped to an energy state created by an impurity of the lattice, the value of γ is approximately 3 [17]. It is important to note that from Equation 2.17 is that the lower the band gap energy, the stronger the temperature dependency. In multi-junction architectures each subcell has its own temperature dependent decrease in V_{oc}, and the total dV_{oc} is the sum of the dV_{oc} of the subcells. This means that adding junctions to a multi-junction solar cell increases the absolute voltage drop with increasing temperature. However, the total voltage of the cell increases also. Therefore, the relative temperature sensitivity (change in voltage with respect to the total voltage) is smaller with more junctions.

The band gap of the semiconductor material is also sensitive to temperature. The temperature dependency of the band gap is given by the Varshni relation

$$E_g(T) = E_{g,0} - \frac{\alpha T^2}{T + \beta}, \tag{2.18}$$

where $E_{g,0}$ is the band gap energy at 0 K, T is the temperature and α and β are material dependent properties. The band gap energy is thus lowered at higher temperatures. This temperature dependency of the band gap translates to temperature dependency of I_{sc}: Because the band gap is lowered and the absorption range is widened, more photons are capable of exciting the electrons to the conductance band. In single-junction cells this is seen as a rise in I_{sc}. In principle this effect is also seen in each subcell of a multi-junction solar cell, but it is not straightforward, as the current balance is dependent on the absorption and current produced by other subcells. Because the intensity of the sun is not independent of the wavelength, in a multi-junction configuration the change in band gaps result in a shift in the current balance. Thus, the limiting subcell at T=25 °C might not be the limiting subcell at T=80 °C.

The fill factor is also sensitive to temperature, and most of it originates from the

temperature dependency of V_{oc} described earlier. The dependency is negative i.e. the FF decreases with increasing temperature. However, for multi-junction solar cells expressing the temperature dependency of FF analytically is challenging, due to it being dependent on the level of current mismatch, which is further dependent on the operating conditions.

3. HEAT TRANSFER

Heat transfer methods are generally divided into three categories: conduction, convection and radiation. In this section the main physics of these heat transfer methods are described, as they all play a role in cooling down a CPV cell.

3.1 Conduction

On a microscopic scale, heat is vibrating movement of atoms and molecules. When a molecule or atom vibrates in a solid, it interacts with its neighbouring atoms resulting in an exchange of kinetic energy. This mechanism is known as conduction. This requires the existence of a temperature gradient: the heat is transferred from the higher temperature region to the lower temperature region, as stated by the second law of thermodynamics. Conduction takes place in solids, liquids and gases. [13, pp. 20–21]

The rate at which heat conducts through a medium depends on the geometry as well as the thermophysical properties. In general, the heat transfer rate per unit area is proportional to the normal temperature gradient, which can be expressed in one-dimensional case as

$$\frac{Q}{A} \propto \frac{\partial T}{\partial x} \,. \tag{3.1}$$

This is usually expressed with proportionality constant k as

$$Q = -kA\frac{\partial T}{\partial x} \,, \tag{3.2}$$

where Q is the heat transfer rate, A is the cross-sectional surface area, $\frac{\partial T}{\partial x}$ is the temperature gradient in the direction of the heat flow and k is a positive constant called thermal conductivity with a unit of $[\frac{W}{m \cdot K}]$ [25, p. 2]. Equation 3.2 is also known as Fourier's law, which is usually written in differential form

$$\overrightarrow{Q} = -k\nabla T\,, \tag{3.3}$$

where $\overrightarrow{Q}$ is the local heat flux density and ∇T is the temperature gradient.

Thermal conductivity is a material property, that can be defined as *"the rate of heat transfer through a unit thickness of the material per unit area per unit temperature difference"*, as described by Y. A. Çengel [13, p. 22]. Materials with high thermal conductivities are good heat conductors, whereas low thermal conductivity materials are considered insulators. Thermal conductivity varies hugely between different materials, as is seen in Table 3.1. As thermal conduction is a result of the vibrational motion of the atoms, it is apparent that the thermal conductivity is not independent of the temperature [25, pp. 6–7].

Table 3.1 *Thermal conductivities of various materials at 300 K*

Material	**Thermal conductivity k** $[W/m \cdot K]$
Diamond [21]	2400-2500
Copper [43]	401
Aluminum [43]	237
Gallium arsenide [30]	52
Germanium [20]	60
Silicon [20]	84
Water [38]	0.6096
Air [49]	0.026
Argon [29]	0.018

In general, gases have low values of thermal conductivities. The kinetic theory of gases can predict their thermal conductivities, which considers the collisions between atoms and molecules as the prime method for heat transfer. In general, it is proportional to the square root of the absolute temperature and inversely proportional to the square root of the molar mass. Therefore, the thermal conductivity of a gas rises as the temperature rises [13, p. 25]. This is intuitive, considering that high temperature gas molecules have higher mean velocity, resulting in collisions to occur more often. Liquids have slightly higher thermal conductivities than gases, as the molecules in a liquid are more tightly spaced. Solids on the other hand have the highest thermal conductivities, which is explained by their atomic structure. In solids heat is conducted via vibrational waves along the lattice or via free electrons. Metals are good electrical conductors due to a lot of free electrons in their structure. Thus, their thermal conductivities are also high. However, highest thermal conductivities are found in materials that have highly ordered crystalline structures (such

as diamond), and the heat is transferred primarily by lattice vibrations.

In heat conduction heat is not only conducting from hot area to cold area, but it is also stored into the medium. Thus, in heat transfer analysis it is common to define *thermal diffusivity D*, which is a measure of transient thermal response of a material to a change in temperature. It is defined as

$$D = \frac{k}{\rho c_p}\,, \tag{3.4}$$

where k is the thermal conductivity, ρ is the density and c_p is the specific heat capacity. Thermal diffusivity could be interpreted as the materials ability to conduct thermal energy relative to its ability to store thermal energy. Another way of interpreting thermal diffusivity is to think it as a measure of thermal inertia, i.e. how fast a temperature concavity is smoothed out.

3.2 Convection

In solids, heat transfer always occurs by conduction since the atoms are in fixed positions. However, in a fluid atoms can move freely, and thus heat transfer in a fluid also involves motion of the atoms. In general, this movement of molecules and atoms within a fluid is known as convection. In thermodynamics, convection refers to the heat transfer mechanism based on convection. In a fluid, a rise in temperature typically results in lower density. This causes a motion within the fluid where the less dense fluid will start to rise. This motion is called natural convection. In contrast to natural convection, the convective heat transfer can also be forced. In forced convection the movement of the fluid is caused by an external force.

The base mechanism of convective heat transfer still lies in conduction; a fluid near a heated surface will start to heat up due to heat gradient near the surface. However, the temperature gradient is dependent on the velocity of the fluid; a high velocity fluid produces a large temperature gradient near the interface, whereas a stationary fluid has a smaller gradient. Thus, a fluid flowing with high velocity cools the surface down more effectively.

The overall heat transfer caused by convection can be expressed with Newton's law of cooling

$$Q = HA(T_s - T_{env}), \tag{3.5}$$

where A is the surface area between the wall and the fluid, T_s is the temperature of the surface, T_{env} is the temperature of the environment and H is the *convective heat transfer coefficient*. The exact value for H can be calculated analytically for some systems, but in most cases it must be determined experimentally. [25, p. 12]

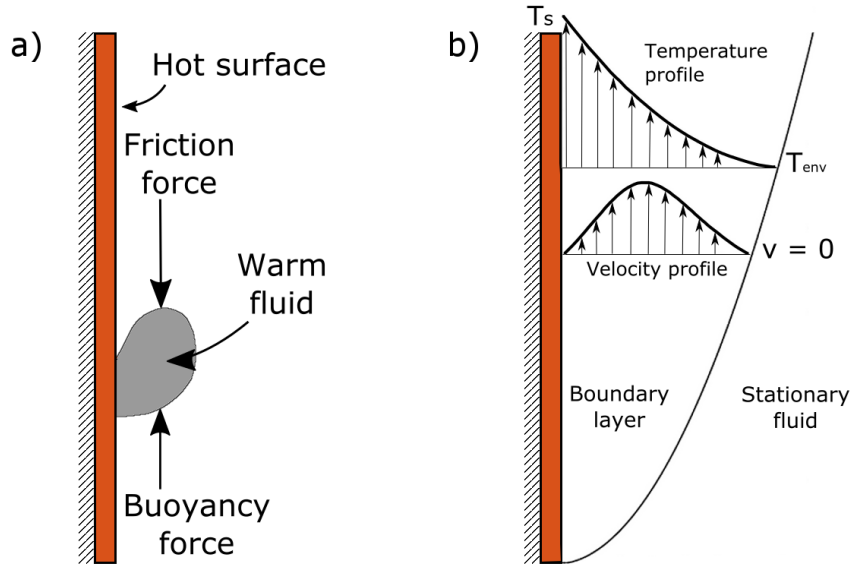

Figure 3.1 *a) Forces acting upon warm fluid near a hot surface. b) Formation of a boundary layer near a hot surface and typical velocity and temperature profiles for fluid near a heated vertical surface.*

In general, there are two forces that act upon the heated fluid; friction forces caused by the kinematic viscosity of the fluid near a surface and buoyant forces that are caused by the density difference between the heated fluid and the fluid surrounding it. These forces are shown in Figure 3.1. The friction force between a fluid and a solid is comparable to the friction force of two solid bodies moving against each other. In addition, the higher the velocity of the fluid, the greater the friction between the fluid and the wall. Under steady conditions the fluid moves at constant velocity, as the friction force and the buoyant force cancel each other out.

One measure of convective heat transfer at a surface is the Nusselt number (Nu), which is defined as the ratio between the rate of convective and conductive heat transfer:

$$Nu = \frac{HL}{k}. \tag{3.6}$$

In Equation 3.6, H is the convective heat transfer coefficient, L is the characteristic length and k is the thermal conductivity of the fluid. The characteristic length has several different definitions and it has to be chosen according to the geometry. Char-

acteristic lengths for some geometries have been listed in Table 3.2. To illustrate the meaning of the Nusselt number, Incropera et. al. [26] describe it the following way: *"The Nusselt number is to the thermal boundary layer what the friction coefficient is to the velocity boundary layer"*. Rearranging 3.6 results in an expression for the convective heat transfer coefficient

$$H = \frac{k}{L} Nu, \tag{3.7}$$

which can be solved numerically, if the Nusselt number is known for the system. For natural convection with empirical corrections, the simplified formula for Nusselt number is found to be

$$Nu = C(Gr\, Pr)^n, \tag{3.8}$$

where C and n are geometry dependent constants, Gr is the *Grashof number* and Pr is the *Prandtl number* [13, p. 416]. For natural convection the Grashof number is defined as the ratio of the buoyancy force and the viscous force, i.e.

$$Gr = \frac{\text{Buoyancy forces}}{\text{Viscous forces}} = \frac{g\phi(T_s - T_\infty)L^3}{\nu^2}, \tag{3.9}$$

where g is the gravitational acceleration, ϕ is the coefficient of volume expansion of the fluid, T_s is the temperature of the surface, T_∞ is the temperature of the fluid outside the boundary layer, L is the characteristic length and ν is the kinematic viscosity of the fluid [13, p. 415]. The Prandtl number describes the relative thickness of the thermal boundary layer shown in Figure 3.1 and is defined as

$$Pr = \frac{\text{Molecular diffusivity of momentum}}{\text{Molecular diffusivity of heat}} = \frac{\mu C_p}{k}, \tag{3.10}$$

where μ is the dynamic viscosity of the fluid, C_p is the specific heat and k is the thermal conductivity [13, p. 356]. Finally, we define *Rayleigh number (Ra)*, which is defined as the product of Grashof number and Prandtl number, reducing Equation 3.8 to

$$Nu = C\, Ra^n. \tag{3.11}$$

Empirical values for Nu are presented in Table 3.2 for different geometries.

Table 3.2 *Empirical corrections for the Nusselt number for natural convection [14, pp. 256–257]*

Geometry	**Characteristic length** (L)	**Range of Ra**	**Nusselt number** (Nu)
Inclined plate at an angle θ $-60° < \theta < 60°$	Plate length	$\leq 10^9$	$0.68 + \frac{0.67((cos\,\theta)Ra)^{1/4}}{\left(1+\left(\frac{0.492}{Pr}\right)^{9/16}\right)^{4/9}}$
		$> 10^9$	$\left(0.825 + \frac{0.387Ra^{1/6}}{\left(1+\left(\frac{0.492}{Pr}\right)^{9/16}\right)^{8/27}}\right)^2$
Vertical plate	Plate length	$\leq 10^9$	Use inclined plate equation with $\theta = 0°$.
		$> 10^9$	Use inclined plate equation.
Horizontal plate	$\frac{\text{Plate area}}{\text{perimeter}}$		
a) Upper surface of a hot plate		10^4–10^7	$\text{Nu} = 0.54\ \text{Ra}^{1/4}$
		10^7–10^{11}	$\text{Nu} = 0.15\ \text{Ra}^{1/3}$
b) Lower surface of a hot plate		10^5–10^{11}	$\text{Nu} = 0.27\ \text{Ra}^{1/4}$

In forced convection the motion of the fluid on the cooling surface is caused by an external force. Even though cooling by forced convection obeys Newton's law (see Equation 3.5), it is still rather complex as the heat transfer coefficient H depends on many fluid properties. In forced convection we are interested in the type of the flow: it can be turbulent or laminar. This is dependent on the inertia forces and viscous forces within the fluid. To determine whether the flow is laminar or turbulent, a *Reynolds number* (Re) is usually defined:

$$Re = \frac{\text{Inertia forces}}{\text{Viscous forces}} = \frac{v_\infty L}{\nu}, \tag{3.12}$$

where v_∞ is the fluid velocity outside the boundary layer, L is the characteristic length of the geometry and ν is the kinematic viscosity of the fluid [13, p. 355]. The point where laminar flow turns into turbulent flow is defined as the critical Reynolds number. For a flat plate the value for $Re_{\text{critical}} \approx 5 \cdot 10^5$.

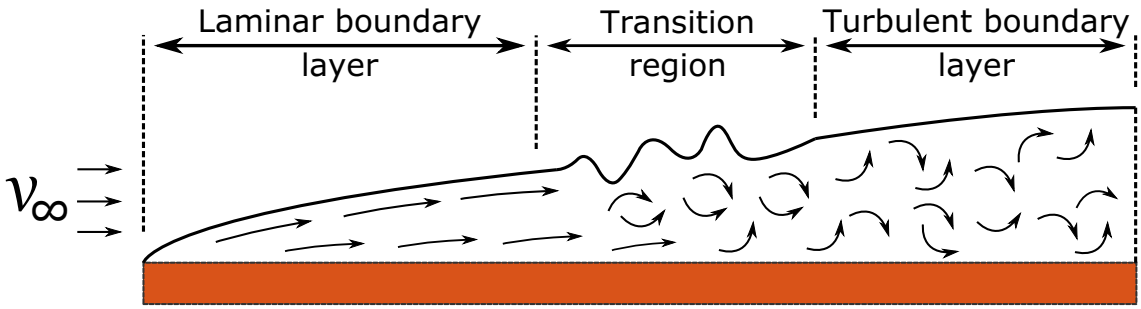

Figure 3.2 *The development of different flow regimes for flow over a flat plate.*

Let's consider a flat horizontal plate, where fluid approaches the plate from left to right in x-direction with a velocity of v_∞. The velocity boundary layer can be divided into three components: Laminar boundary layer, turbulent boundary layer and a transition region between the two. These are shown in Figure 3.2. The friction at the fluid-plate interface causes a force to the fluid in the opposite direction of the flow. The fluid flowing above this layer causes a dragging force (shear stress) to the fluid beneath. A boundary layer region, where the friction force affects the velocity, is formed. Outside this region the frictional effects are negligible, and the velocity is close to constant. For the laminar flow region i.e. $Re \leq 5 \cdot 10^5$ the local Nusselt number Nu_x is found to be

$$Nu_x = \frac{0.3387 Pr^{1/3} Re^{1/2}}{\left(1 + \left(\frac{0.0468}{Pr}\right)^{2/3}\right)^{1/4}}. \tag{3.13}$$

for all Prandtl numbers [26, p. 410]. In the turbulent flow region the local Nusselt number is

$$Nu_x = 0.0296 Re^{4/5}\, Pr^{1/3}, \tag{3.14}$$

if $0.6 \leq Pr \leq 60$ and $5 \cdot 10^5 \leq Re \leq 10^7$ [26, p. 411]. For combined laminar and turbulent flow, the Nusselt number is defined as

$$Nu_x = (0.037 Re^{4/5} - 871)\, Pr^{1/3}, \tag{3.15}$$

if $0.6 \leq Pr \leq 60$ and $5 \cdot 10^5 \leq Re \leq 10^7$ [26, p. 412]. Due to different flow regions, it is apparent that the heat transfer coefficient is not constant along the surface. Thus average heat transfer coefficients are usually defined for a surface.

The average Nusselt numbers $\overline{Nu}$ from local Nusselt number Equations 3.13, 3.14 and 3.15 are obtained by $\overline{Nu} = 2Nu_x$ [26, p. 410].

When solving a cooling problem with forced convection, the first thing is to calculate Re for the system and determine whether the flow is laminar or turbulent. If $Re < 5 \cdot 10^5$, we use relation for laminar flow. In other cases, either turbulent or combined relations can be used.

3.3 Radiation

When an opaque body is irradiated, part of the irradiation is reflected and the rest is absorbed. The absorbed energy increases the translational kinetic energy of the atoms in the body, which causes a rise in temperature. However, as the atoms are vibrating, the electrical charges in the atom are also accelerated. According to the electromagnetic theory, all moving charges emit electromagnetic radiation, thus causing all objects with temperature above absolute zero to emit electromagnetic radiation. The kinetic energy of the atoms and molecules is converted into electromagnetic energy [47]. A black body is an ideal object that absorbs all electromagnetic radiation at all wavelengths. When at uniform temperature, a black body emits a characteristic spectrum (Figure 3.3) of electromagnetic radiation to its surroundings. The energy distribution of this emission spectrum as a function of wavelength and temperature is given by Planck's law

$$I_{\lambda,b}(\lambda, T) = \frac{2hc^2\lambda^{-5}}{e^{hc/\lambda k_B T} - 1}, \tag{3.16}$$

where c is the speed of light in the medium, h is the Planck constant and k_B is the Boltzmann constant. According to Incropera et. al. [26, pp. 728–729], equation 3.16 gives us *"...the rate at which radiant energy is emitted at the wavelength λ in the (θ, ϕ) direction, per unit area of the emitting surface normal to this direction, per unit solid angle about this direction and per unit wavelength interval $d\lambda$ about λ."* Equation 3.16 can thus be rewritten as

$$I_{\lambda,e}(\lambda, \theta, \phi) = \frac{dq}{dA_1 \cos\theta \, d\omega \, d\lambda}\,, \tag{3.17}$$

$$\frac{dq}{d\lambda \, dA_1} = I_{\lambda,e}(\lambda, \theta, \phi) \cos\theta \, d\omega\,. \tag{3.18}$$

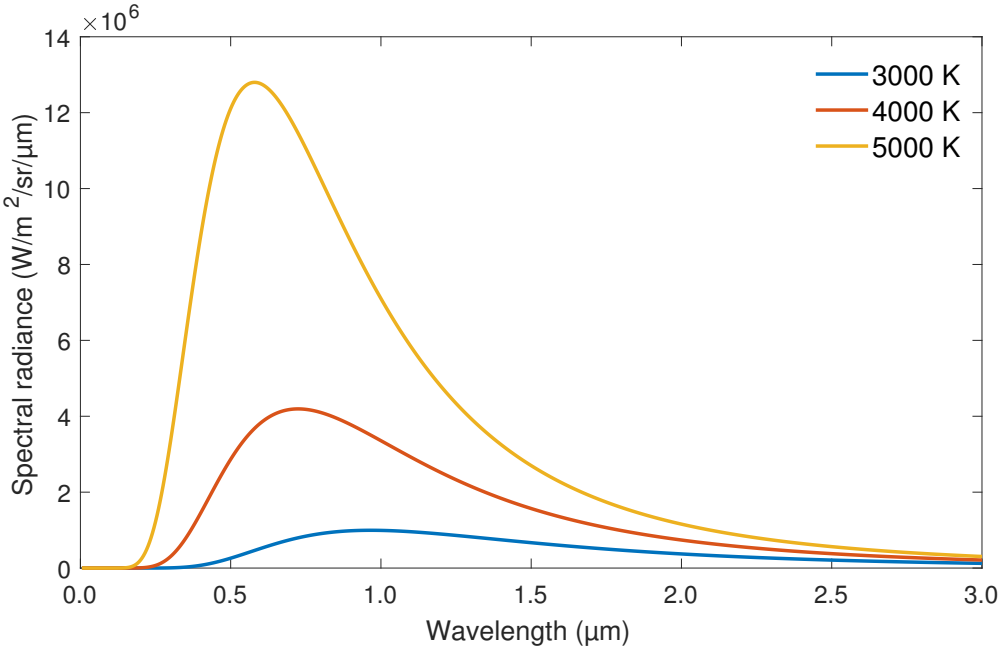

Figure 3.3 *Black-body radiation emitted by ideal black bodies with different temperatures.*

To calculate the total emission power of a black body, let's consider a flat surface. The surface element dA_1 emits radiation in a half-sphere above the surface. The differential solid angle $d\omega$ can be expressed as

$$d\omega = sin\,\theta\,d\theta\,d\phi. \tag{3.19}$$

Substituting this to equation 3.18 yields

$$\frac{dq}{d\lambda\,dA_1} = I_{\lambda,e}(\lambda,\theta,\phi)\,cos\,\theta\,sin\,\theta\,d\theta\,d\phi, \tag{3.20}$$

If the spectral and directional properties of the $I_{\lambda,e}$ are known, the overall emission power over the half sphere can be calculated from

$$\frac{E(\lambda)}{d\lambda} = \int_0^{2\pi}\int_0^{\frac{\pi}{2}} I_{\lambda,e}(\lambda,\theta,\phi)\,cos\,\theta\,sin\,\theta\,d\theta\,d\phi. \tag{3.21}$$

In case of *diffuse emitter*, which we are considering here, the intensity of emitted radiation is independent of the angle, i.e. $I_{\lambda,e}(\lambda,\theta,\phi) = I_{\lambda,e}(\lambda)$. Thus the integration results in

$$\frac{E(\lambda)}{d\lambda} = \pi I_{\lambda,e}(\lambda) \tag{3.22}$$

Substituting equation 3.16 to 3.22 and integrating over all wavelengths yields

$$E(\lambda) = \pi \int_0^\infty \frac{2hc^2\lambda^{-5}}{e^{hc/\lambda k_B T} - 1} d\lambda \tag{3.23}$$

$$E(\lambda) = 2\pi hc^2 \int_0^\infty \frac{d\lambda}{\lambda^5 (e^{\frac{hc}{\lambda k_B T}} - 1)}. \tag{3.24}$$

$$E = \frac{2\pi^5 k_B^4}{15h^3c^2}\, T^4 = \sigma\, T^4 \tag{3.25}$$

which is known as Stefan-Boltzmann law and σ is known as *Stefan-Boltzmann constant* with a value of $5.67 \cdot 10^{-8}[W/m^2 \cdot K^4]$. Equation 3.25 gives the total power per unit area emitted by an ideal black body surface. However, as no ideal black body exist, we define ϵ as the ratio of radiative power emitted by a real body to the radiative power emitted by a black body, i.e.

$$\epsilon = \frac{E_{\text{real body}}}{E_{\text{black-body}}}\,, \tag{3.26}$$

where ϵ is known as emissivity. Emissivity is a property of a material which defines how well the material absorbs and emits black-body radiation. It is usually dependent on the surface material and morphology. By combining Equations 3.25 and 3.26 we get the power per unit area emitted by a real body

$$E_{\text{real body}} = \epsilon\, E_{\text{black-body}} = \epsilon\, \sigma\, T^4\,. \tag{3.27}$$

In essence, heat transfer by radiation is not only about a body emitting radiation to its surroundings, but also absorbing black-body radiation from its surroundings. Because practically all objects emit black-body radiation, we are interested in the net energy exchange between an object and its surroundings. Thus, it is common to express the net radiative power per unit area E_{net} as

$$E_{net} = E_{out} - E_{in} = \epsilon\, \sigma\, T^4 - \epsilon\, \sigma\, T_{amb}^4 = \epsilon\, \sigma\, (T^4 - T_{amb}^4)\,, \tag{3.28}$$

where E_{out} is the power per unit area emitted by the body, E_{in} is the power per unit area emitted by the surroundings and T_{amb} is the ambient temperature.

4. RESEARCH METHODOLOGY

The research conducted in this thesis consists of two methods: solar cell measurements and finite element method (FEM) simulations. As this thesis focuses in simulations considering heat management of CPV cells, the measurements are mainly used to validate the simulation models.

4.1 Current-voltage measurements

The electrical performance of solar cells are usually determined by measuring their current-voltage characteristics. To obtain the characteristic figures of merit (see Figure 2.4) for a cell, the cell has to be illuminated. However, the spectral properties of the incoming sunlight greatly affect the performance of the solar cell, as discussed in section 2.3. Thus, using random light source to measure the cell is not acceptable. To simulate the operation under real sunlight, so called solar simulators are usually used. With a xenon lamp as a light source and with appropriate filters applied to the beam, the spectrum of the sun can be matched reasonably well. [22]

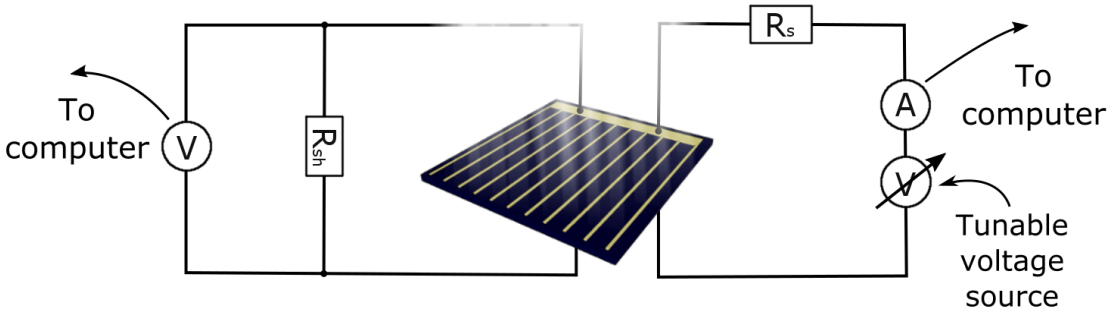

Figure 4.1 *A schematic of a typical IV-measurement setup with four-point contact. The voltage across the terminals can be adjusted with a tunable voltage source.*

A typical solar cell measurement setup is illustrated in Figure 4.1. The cell is illuminated with the light source and a variable voltage source sweeps through a range of voltages. The current passing through the cell and the voltage across the terminals are measured and recorded during the sweep, and they are used to analyse the performance of the cell. A four-point contact measurement is typically used to

eliminate the unwanted effects of contact resistance and the series resistance caused by the test leads. To keep the testing conditions stable, a controllable thermoelectric cooler is usually placed under the cell. The standard testing conditions are 25 °C and 28 °C, of which the former is used in this thesis. [22, pp. 99–100]

In this thesis the cells were measured with an OAI CPV HD1500 solar simulator. The simulator is equipped with a xenon short arc lamp as a light source, and a spectral filter to match the solar spectrum. The simulator has a designated light guide for concentration measurements. The size of the illuminated area at the end of the light guide is $15 \times 15\ mm^2$, and a concentration of roughly 1000 suns can be reached with the system. The illumination of the simulator is controlled by a shutter. The shutter is opened at the beginning of the measurement. After a delay of 0.10 s, the V_{oc} is measured by setting the power supply to zero current output. Then, the I_{sc} is measured by setting the adjustable voltage source to zero voltage output. These two properties measured 0.10 s after the shutter has been opened, will be called from this point forward the *direct open circuit voltage* (V_{ocd}) and *direct short circuit current* (I_{scd}), as they are measured directly. After a short delay, the actual voltage sweep is performed to measure the current of the cell at a range of voltages. From the measured values we can draw an IV-curve which can be used to determine the I_{sc} and V_{oc} by fitting a line locally around the x-axis and y-axis intercepts. The I_{sc} and V_{oc} are calculated from the fit. At 500 Hz data acquisition rate, the V_{oc} is measured 1.77 s after the shutter has been opened. It is apparent, especially at higher concentrations, that the temperature of the cell increases during a measurement. This can be easily seen as the difference between V_{ocd} and V_{oc}, which gives us one tool to analyse the operating temperature of the cell during the measurement.

4.2 Simulations

To date, simulation programs are widely used in both research and product development. One of the purposes of using a simulation software is to reduce the number of prototypes and experiments during the design and manufacturing processes. In addition, this usually translates to lower development costs. Once a model that can predict real-life properties has been built, it can be used for example to prototype new designs or improve an existing one. In this thesis simulations are used to predict heat management requirements for a CPV system. This could be applied for example to design guidelines.

4.2.1 Finite element method

The finite element method (FEM) is a numerical method used to obtain approximate solutions to physical problems. FEM is especially good for solving real-life problems, where the geometries are complex and the physics requires solutions for partial differential equations. The mathematical background theory of FEM is well developed and a more profound basis can be found e.g. from reference [12]. Here we take only a glance over the theory behind FEM.

Many space- and time-dependent problems are usually expressed in terms of partial differential equations (PDE). In general, PDE:s are equations that determine the rate of change in a dependent variable with respect to independent variables. Most PDE:s cannot usually be solved analytically in real-life geometries. To tackle this problem, in the finite element method the given domain is divided into subdomains or elements, like in Figure 4.2. This discretisation of the domain offers approximate solutions to the PDE:s, which can be solved numerically using approximating functions.

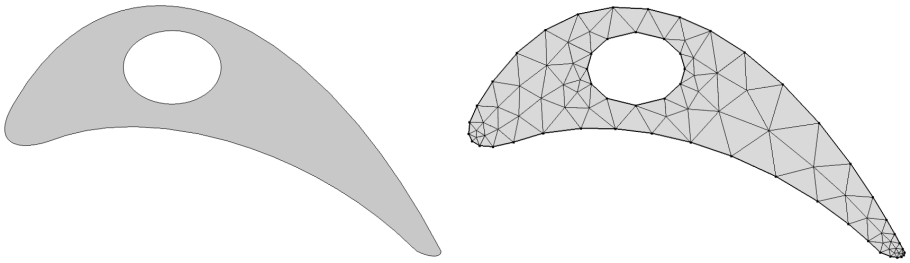

Figure 4.2 *Finite element discretisation of a domain.*

Let's look at an example function u, which is a variable in a PDE. The function u can be approximated by another function u_h. We can construct u_h as a linear combination of basis functions, i.e.

$$u_h = \sum_i u_i \psi_i \,, \tag{4.1}$$

where u_i is the coefficient that approximates u with u_h and ψ_i denotes the basis function. This approximation is illustrated in Figure 4.3 for a simple one-dimensional case. Here the basis functions are 1 at their respective nodes and 0 at other nodes i.e. they are linear. The basis functions can also be non-linear, but they are usually chosen to be polynomial. The basis functions are often called *interpolation functions*, as the values between u_i and u_{i+1} are given by interpolation. The nodes in

Figure 4.3 are uniformly spaced, but the discretisation can also be done unevenly, which is one of the strengths of FEM. [15] In FEM we seek for an approximation to the solution over each element. Then the parts are assembled together, and the solution is obtained for whole system.

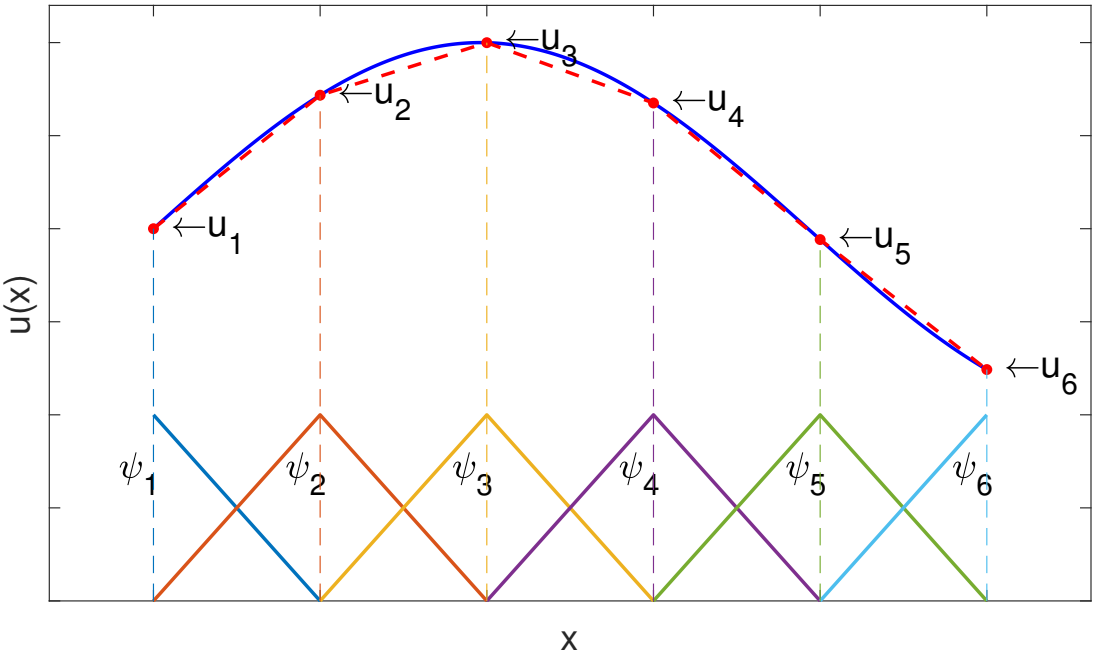

Figure 4.3 *Approximation of function u (in blue) in terms of approximation coefficients u_i and linear basis functions ψ_i. The approximating function u_h is marked with red dashes.*

However, solutions to PDE:s are usually not unique. This means, that without any information about the system we cannot find explicit solution. Thus, boundary conditions must be specified according to the system. Let's consider heat transfer in a solid block. Let's say that for the bottom surface (domain Ω_1) the temperature is a known constant T_0, and at the upward facing surface (domain Ω_2) there is conductive heat transfer present. Other surfaces (domain Ω_3) are insulated. Thus, we can present the boundary conditions for this system as follows:

$$\begin{aligned} T &= T_0 && \text{on } \Omega_1 \\ (-k\nabla T)\cdot\mathbf{n} &= h(T - T_{amb}) && \text{on } \Omega_2 \\ (-k\nabla T)\cdot\mathbf{n} &= 0 && \text{on } \Omega_3 \end{aligned}$$

The outward unit normal vector to the boundary surface is denoted with $\mathbf{n}$. [15] By defining the boundary conditions, the PDE:s in the system can be solved. However, the derivation of a solution for even one-dimensional heat transfer system is mathematically complex, and the derivation can be found e.g. from source [50].

COMSOL Multiphysics is a commercially available FEM analysis software, which is used for simulating heat transfer problems in this thesis. Through a graphical user interface the user can create simulation models. Currently there are over 20 modules for modelling different physical phenomena ranging from electrical and mechanical problems to fluid flow and optics. In this thesis, only the heat transfer module is used. To create a simulation model, the user must first define which physics are simulated. Secondly, a simulation geometry must be created. For each body in the geometry, the user can either select materials from a built-in materials library, or define the material properties by hand. For the simulation to converge, boundary conditions must be set for each domain. In the heat transfer module, boundary conditions can be e.g. constant temperature, insulation, heat flux or diffuse surface. In addition, it is possible to define variables which are dependent on surface or body temperature. This is especially useful when the efficiency of the modelled solar cell is dependent on the body temperature, and should be evaluated according to the temperature separately at each point. It is also possible to perform parametric sweeps, where a parameter (e.g. concentration) value can be varied over a range of values. Lastly, in COMSOL it is possible to simulate both time-dependent and stationary systems. In this thesis, both are used.

4.2.2 Simulation constraints

To calibrate the simulations with measurements, certain parameters have been chosen as constants. These constants are presented in Table 4.1. The spectrum, and the direct normal irradiance (DNI) derived from it, are based on the OAI solar simulator. The ambient temperature T_{amb} used in the simulations is roughly the same as the ambient temperature in the solar simulator laboratory where the cells are measured. This is also the standard test atmosphere defined for solar cell testing [22]. For the case studies, an optical efficiency of $n_{opt} = 0.85$ has been chosen based on the current state of development of concentrator optics [10, 52, 4].

Table 4.1 *Simulation constants*

Name	Value	Description
I_{sun}	1000 W/m^2	DNI
S	AM1.5D	Spectrum
T_{amb}	25 °C	Ambient temperature
n_{opt}	0.85	Optical efficiency

As described in Chapter 3, the heat transfer mechanisms are dependent on material properties. To reduce the amount of adjustable parameters within simulations, thermophysical parameters presented in Table 4.2 are used in all of the simulations.

For a heat conduction model, we need the thermal conductivity, heat capacity and density of each material. For radiative cooling, the emissivity of the material is needed. The emissivity of the solder is not needed as it is defined as a thin layer between the cell and the package in COMSOL.

Table 4.2 *Thermophysical parameters used in simulations for different materials.*

Material	$k[W/m \cdot K]$	$C_p(J/kg \cdot K)$	$\rho(kg/m^3)$	ϵ
Copper	400	385	8700	0.05
Aluminum	238	900	2700	0.10
Germanium	60	320	5323	0.90
Steel	44.5	475	7850	0.10
Al_2O_3	30	900	3900	0.75
$Sn_{96.5}/Ag_{3.0}/Cu_{0.5}$ solder [27]	73	250	7500	-

Table 4.3 *Temperature coefficients of the 3C44 solar cell [6].*

Parameter	$\Delta I_{sc}/\Delta T$	$\Delta V_{oc}/\Delta T$	$\Delta P_{mp}/\Delta T$	$\Delta\eta/\Delta T$
Value	0.6 mA/K	-4.2 mV/K	-2.1 mW/K	-0.046%/K

Unless otherwise stated, the solar cell used in the measurements and simulations of this thesis is a commercially available 3C44 Concentrator Triple Junction Cell manufactured by AZUR SPACE Solar Power GmbH [6]. This cell was chosen for the calibrations, since the temperature dependencies of the cell are well known (see Table 4.3). A simple model for the temperature and concentration dependency of the efficiency can be formulated from the known parameters. The reported efficiencies as a function of concentration are presented in blue in Figure 4.4. The efficiency has roughly a 2nd degree polynomial dependency on concentration at T=25 °C. Because the temperature dependency of efficiency is linear (see Table 4.3), we can deduce a formula for efficiency as a function of concentration and temperature:

$$\eta(X,T) = (-3 \cdot 10^{-8} X^2 + 2 \cdot 10^{-5} X + 0.4343) - 0.00046 \, \frac{1}{K} \cdot (T - 298.15\,K)\,. \quad (4.2)$$

The line plotted in red in figure 4.4 presents the efficiency at T=80 °C, which was calculated from Equation 4.2. Equation 4.2 will be utilised in the simulations, where the efficiency of the cell needs to be calculated at each simulation step based on the temperature and concentration.

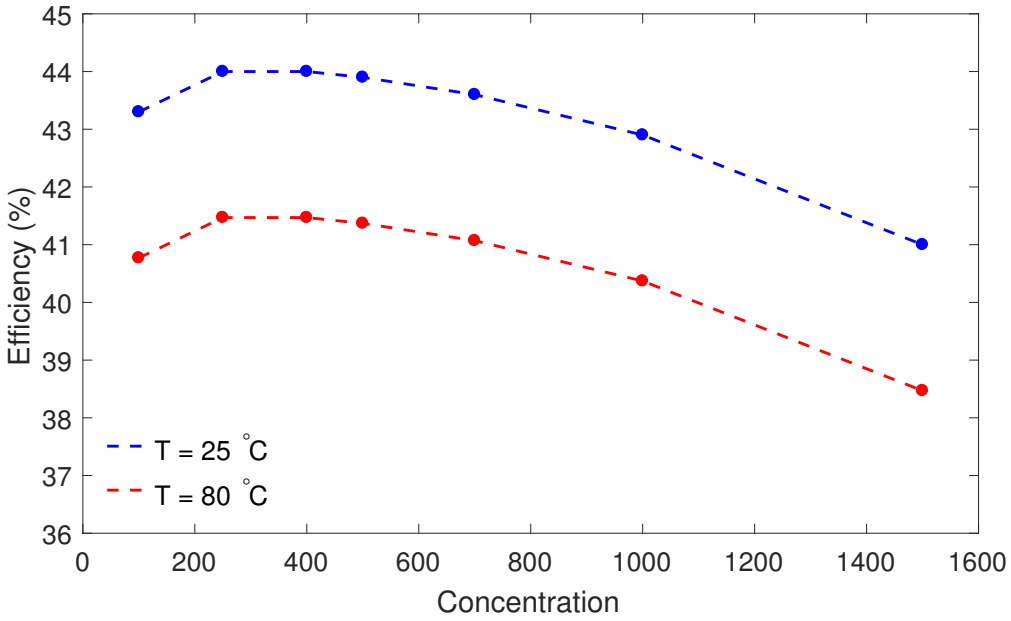

Figure 4.4 *Efficiency of 3C44 solar cell as a function of concentration at two different temperatures.*

4.2.3 Packaging geometries and simulation boundary conditions

In this thesis two types of solar cell packages are considered. Firstly, in simulations regarding the measurements, a copper heatsink with a solder paste bonded cell is used. The copper heatsink is in thermal contact with a thermoelectric cooled heatsink made of steel. The geometry of this package is shown in Figure 4.5. As discussed in Section 4.1, the illuminated area in an OAI solar simulator measurement is $15 \times 15\ mm^2$. The illuminated area is sketched in Figure 4.5 to illustrate the size of the illuminated area compared to the size of the cell. The dimensions of this assembly are presented in Table 4.4.

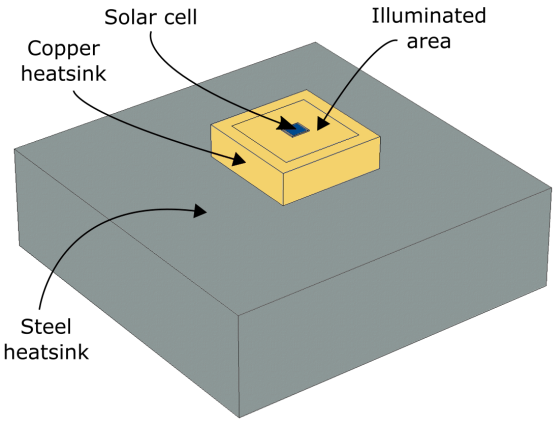

Figure 4.5 *CAD drawing of the cell package used in the measurements.*

Table 4.4 *Dimensions of solar cell packages*

Layer	Thickness (mm)	Width (mm)	Length (mm)
Measurement package			
Copper heatsink	6.00	20.0	20.0
Steel heatsink	19.0	63.6	63.6
Al_2O_3 **substrate**			
Copper	0.10	11.8	13.1
Al_2O_3	0.38	12.4	13.7

Secondly, a substrate consisting of aluminum oxide (Al_2O_3) and copper is considered. This assembly is presented in Figure 4.6. The Al_2O_3 substrate is sandwiched between two thin directly bonded copper (DBC) layers. The copper has metallic traces etched to it in order to isolate the two terminals of the solar cell. In addition, the surface is finished with a Ni/Au plating to prevent surface oxidation. The dimensions of this assembly are also presented in Table 4.4. This substrate is used in all case studies. Due to its relatively low manufacturing costs, high thermal stability and excellent electrical isolation, it can be considered as the standard CPV package. This substrate is widely used in both publications considering thermal management in CPV (see [46, 32]) and in commercial CPV products (see [7, 45]). In addition, the coefficient of thermal expansion matches closely with germanium, making the package able to withstand thermal cycles.

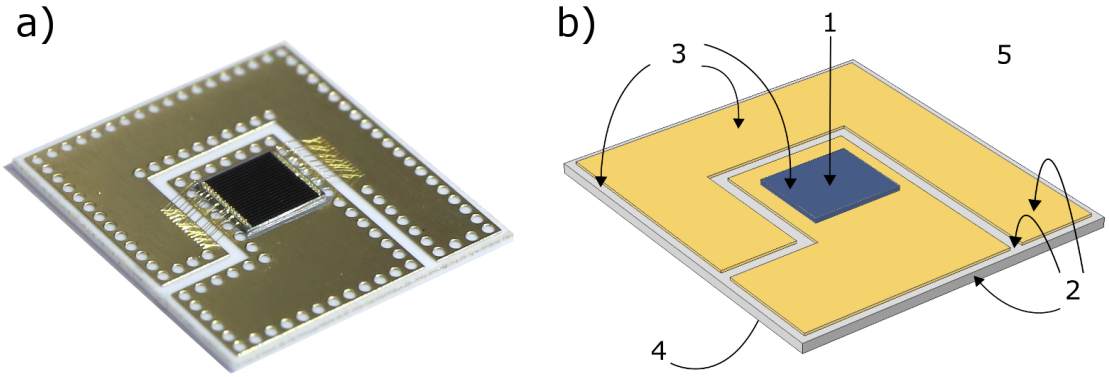

Figure 4.6 *a) A 3C44 solar cell bonded onto an Al_2O_3 DBC substrate. b) The geometry of an Al_2O_3 substrate used in simulations. The numbers refer to the boundary conditions presented in Table 4.5.*

COMSOL Multiphysics offers a comprehensive interface for modelling heat transfer in solids, fluids and porous media. All methods of heat transfer (conduction, convection and radiation) can be taken into account. In addition, surface-to-surface radiation is also available, which could be useful in simulating solar panel assemblies.

In COMSOL, we must define the boundary conditions for each body. In general, there must always be an ambient temperature defined for the solution to eventually converge. In addition, every body must have an initial temperature. In all simulations certain cooling methods are present unless mentioned otherwise. These methods are summarised in Table 4.5 and refer to the numbers presented in Figure 4.6

Table 4.5 *Boundary conditions*

No	Region	Boundary condition
1	Solar cell	Heat source
2	All free surfaces	Radiative emission
3	All free surfaces on sides and facing upwards	Natural convection
4	Downward facing surface	Thermal contact to heatsink
5	Ambient	Ambient temperature

The solar cell is modelled as a heat source, with a heat dissipation power of

$$Q = \eta_{opt} X I_{sun} A_{cell} (1 - \eta(X, T)), \tag{4.3}$$

where $\eta(X, T)$ is given by Equation 4.2. The input intensity is given by the product of irradiation intensity I_{sun}, concentration factor X and the optical efficiency n_{opt} of the system. The input energy is the input intensity times the illuminated area A_{cell}. From this the energy not converted to electricity is converted to heat.

In all simulations, the package presented in Figure 4.6 is attached to a heatsink with thermal interface material to dissipate heat away from the small package. The cooling methods present at the heatsink are explained more detailed in each section in Chapter 5. In general, the sidewalls of the heatsink are considered insulated with no cooling methods present. This consideration is done to model real life scenarios, where CPV solar cells are packed closely next to each other in a matrix form, and the modelled structure is repeated periodically in lateral dimensions.

4.2.4 Validation of the simulation model

To validate the simulation model, a series of measurements were carried out using the OAI solar simulator. The aim was to determine the solar cell junction temperature during a measurement done with the OAI solar simulator under varying concentrations. As mentioned in section 4.1, the open circuit voltage of the cell

is measured twice, at t=0.10 s and at t=1.77 s. From the difference of these two values we can determine the temperature increase of the junction during the measurement, if the temperature coefficient of V_{oc} is known. However, the cell heats up very rapidly after the shutter has been opened, and we cannot assume that the cell is at T_{amb}=25 °C at t=0.10 s. Thus, from ΔV_{oc} we can only determine the relative temperature increase. The higher the concentration the more the cell heats up during the first 0.10 s after the shutter has been opened. To solve this problem, a time-dependent FEM simulation was used to find out the temperature at t=0.10 s. However, we cannot only extract the temperature at t=0.10 s from the simulation; the simulation has to agree with the measurements also at t=1.77 s, where the temperature is the sum of the absolute temperature at t=0.10 s and the relative temperature rise calculated from ΔV_{oc}. Thus, there will be only one solution, where the simulation temperature will fit the measured temperature at both t=0.10 s and t=1.77 s.

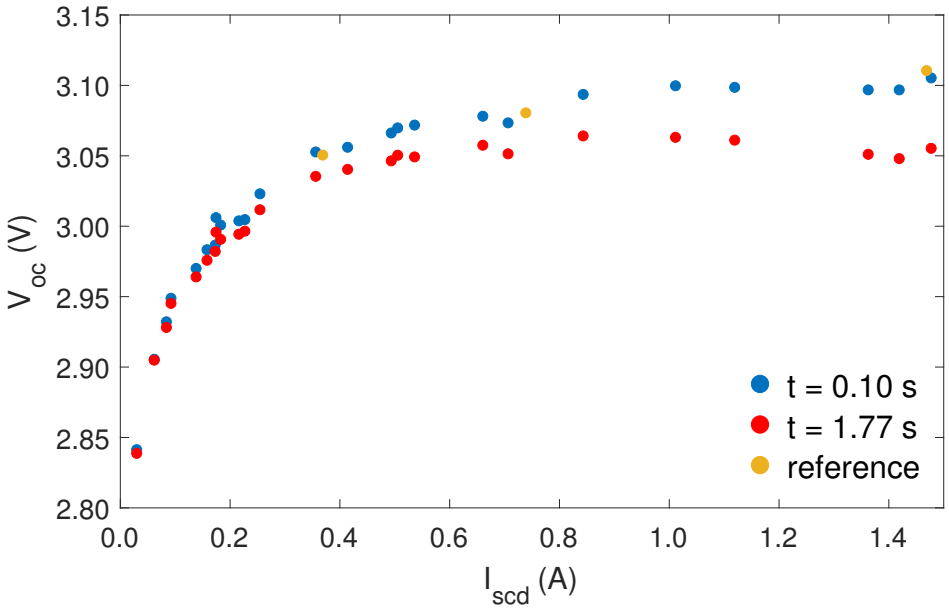

Figure 4.7 *Behaviour of V_{oc} under different concentrations. The voltage difference between the two time points increases as a function of concentration.*

Results from 25 measurements done for the 3C44 cell bonded on a copper heatsink at various concentrations ranging from 20 suns to 1000 suns are plotted in figure 4.7. The x-axis presents the I_{scd} of a single measurement, and in the y-axis is the corresponding V_{oc} values for the same measurement. The V_{ocd} values are plotted in blue, and the V_{oc} values are plotted in red. It is reasonable to assume that the measurement intensity has not changed dramatically during the measurement, and the I_{scd} value can be treated as a constant within a single measurement. The reference values of the 3C44 cell are plotted in yellow. The difference between V_{ocd} and V_{oc} increases as a function of I_{scd} (or concentration), as can be seen in Figure

4.7. In addition, the V_{ocd} measurement data follows the reference values. However, at high concentrations the V_{ocd} should be slightly higher than what is measured. This can be explained by a rise in the operating temperature of the cell.

The $\Delta V_{oc} = V_{ocd} - V_{oc}$ for different values of I_{sc} were calculated from the data shown in Figure 4.7. The results as a function of the I_{scd} are presented in Figure 4.8. As the temperature dependency of the cells V_{oc} is known to be -4.2 mV/K (see Table 4.3), we can calculate the junction temperature increase between the measurements of V_{ocd} and V_{oc} i.e. the relative temperature rise. In addition, the intensity response of the I_{scd} is also known very well, which we can use to roughly determine the concentration of the measurements. Linear regression models were fitted to the calculated differences, which are plotted as red lines in Figure 4.8.

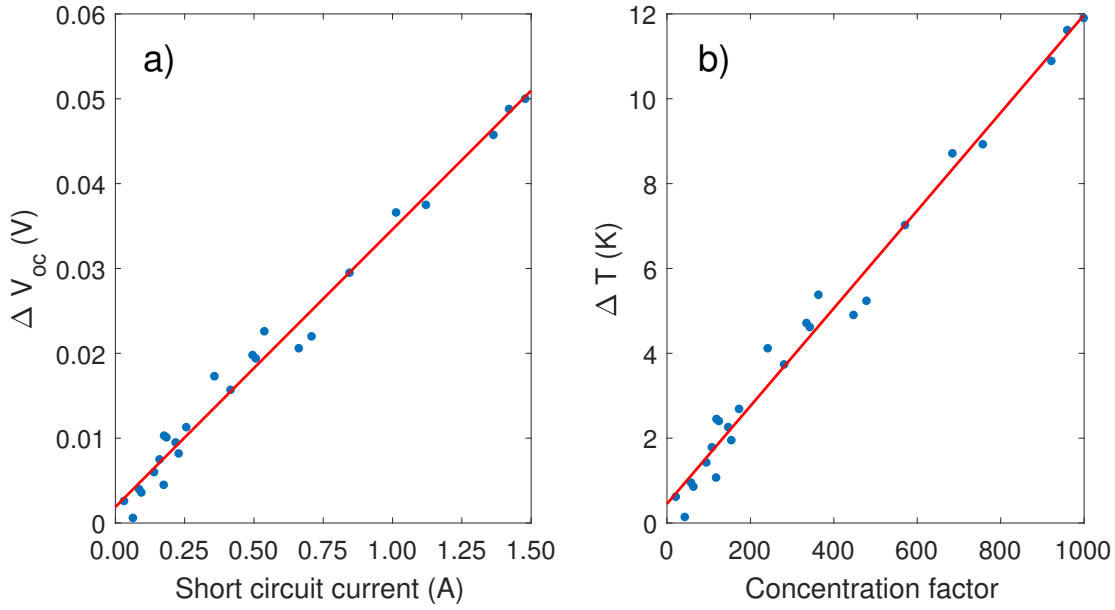

Figure 4.8 *a) ΔV_{oc} as a function of I_{scd}. b) Calculated temperature difference as a function of concentration.*

Now that we know the relative temperature rise as a function of concentration, we can determine the absolute temperature with the aid of a simulation. A time dependent simulation was conducted with constants, geometries and boundary conditions presented in Sections 4.2.2 and 4.2.3. A 2.4 second time period was simulated with concentrations ranging from 200 to 1000 suns. The cell operates at maximum efficiency only when $V = V_{mp}$ during the measurement. Due to the voltage sweep, the cell operates at maximum power point only for a short period of time, and the cell is operating mostly at non-optimal configuration, decreasing the output power of the cell and increasing the heat load. This was taken into account in the simulation by defining a weight function of efficiency, which is zero outside the voltage sweep and reaches unity at the V_{mp}. The weight function decreases rapidly back to zero

after V_{mp}, just like the power-voltage curve of the cell. The operating temperature of the cell is evaluated at the center of the cell at the upward facing surface. This is a reasonably good approximation for the junction temperature, as the junctions lie very close to the surface and are very close to each other. The temperature of the junctions as a function of time at different concentrations is presented in Figure 4.9.

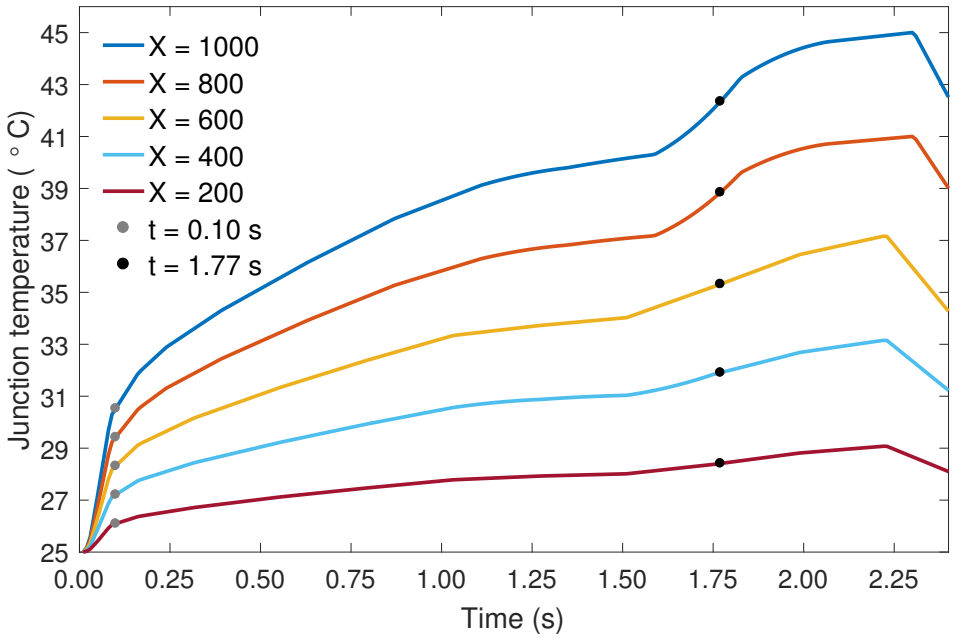

Figure 4.9 *Time dependency of temperature under different concentrations.*

The temperature of the cell increases rapidly during the first 0.25 seconds after the shutter has opened, as we can see from Figure 4.9. After this the temperature rises steadily. The slope starts to decrease from 1.10 seconds onward due to the fact that the cell is in the voltage range where it operates at positive efficiency. The efficiency peaks around 1.55 seconds and then rapidly goes to zero, again increasing the slope. The time points when the V_{ocd} and V_{oc} are measured are shown as grey and black dots in Figure 4.9. The temperature difference (i.e. the separation in y-direction) of the black and grey dot within a single line corresponds to the ΔT presented in figure 4.8.

However, the copper heatsink is in an unknown thermal contact with the steel heatsink. If the contact is considered as ideal, the measurement temperature is underestimated and the simulation will not correspond with the measurements. If we consider the thermal contact to be totally insulated, the temperature is overestimated. These results can be seen in Figure 4.10. Thus, a Cooper-Mikic-Yovanovich correlation (CMYC) was used to model the thermal contact between the heatsinks. The CMYC models the heat flow at the interface of two solid bodies with rough

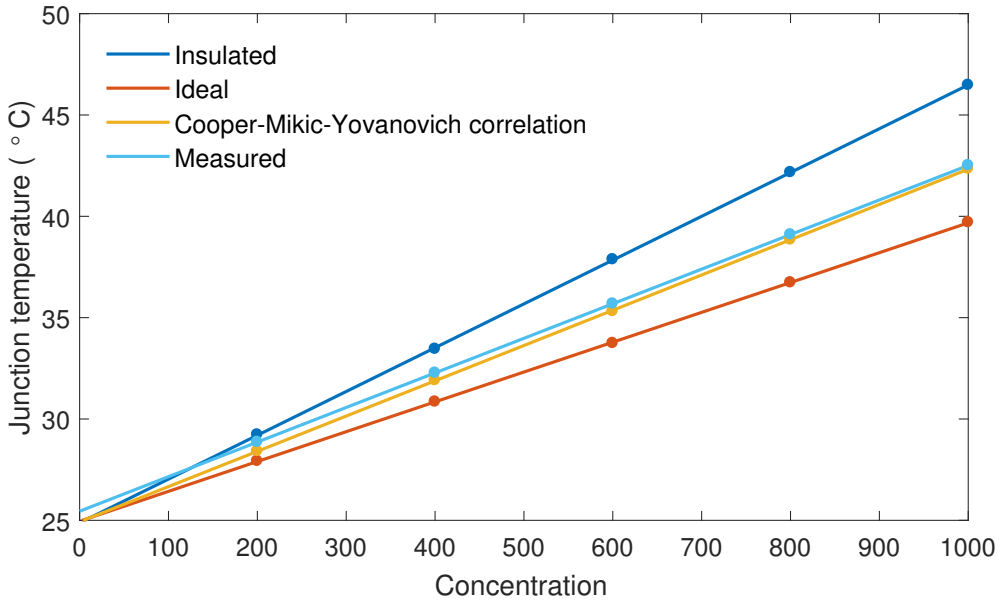

Figure 4.10 *The effect of the thermal contact on the operating temperature at various concentrations.*

contact surfaces. The model assumes plastic deformation of the surface asperities. The theory can be found more detailed in [16]. With CMYC the simulation temperatures match the measured temperatures very closely, as seen in Figure 4.10. This is intuitively the best model for the thermal contact, since we have no thermal interface material between the heatsinks, and the copper heatsink is just lays on top of the steel heatsink. It is important to note that the thermal contact between the heatsinks defines the slope in Figure 4.10, and has no effect on the intercept.

The measured cell is heating up very quickly, and even though the cell is soldered directly to a reasonably big heatsink, the operating temperatures are high compared to the standard test temperature of 25 °C. Thus, the heat management in this measurement setup is not ideal. One problem arises from the solar simulator itself: The illumination beam size is 25 times bigger than the active area of the cell. Even though the gold surface of the copper heatsink absorbs 31% of the incoming irradiation energy, the excessively heated heatsink surface is a remarkable heat source for the measurement package. If the size of the beam would be just about the size of the cell, the junction temperatures would stay well below 32 °C under all concentrations.

The operating temperature of the cell can be estimated very accurately with a COMSOL model. With the boundary conditions defined in Table 4.5 and by modelling the thermal contact adequately, the error between the simulated and the measured temperatures are very small.

5. COOLING STUDIES

In the following sections, different cooling scenarios are considered. First of all, the cooling of a CPV package under passively cooled conditions is investigated. The cooling is based on radiation and natural convective cooling. This is then expanded so, that the convective cooling is forced, which simulates either wind conditions or conditions with cooling fans. After establishing these basic cooling schemes, we will investigate more situational models including cell miniaturisation, space conditions and sub-bandgap photon filtering.

5.1 Passive cooling

In concentrator systems the operating temperature can be very high if the cooling of the cell is not adequate. High temperatures not only decrease the efficiency of the cell, but may even break the cell. Even short failures in cooling may lead to this. In CPV applications passive coolers are considered more reliable, as they are not as vulnerable to system failures as active systems [39, p. 132]. In passive cooling, the cooling is based on natural convection and radiation. Because the cooling power is strongly dependent on the area of the cooling surface, the optics used for concentrating the light set limits to the methods available. The reflective concentrating optics presented in Figure 5.1a, where the cell is positioned between the reflective surface and the sun, is not viable for passive cooling, since the available cooling area is very small. Increasing the cooling area would increase the shadowing losses, making passive cooling an infeasible solution. However, in optical configurations like in Figure 5.1b and 5.1c the whole area of the concentrator is available for cooling, which is ideal [39, p. 133].

To increase the cooling area, finned heatsinks are generally used in power electronics. Bar-Cohen et. al. [8] have proposed a least-material (LM) approach for finned heatsinks balancing the cost and heat dissipation. Micheli et. al. [32] have considered these finned structures for passively cooled solar cell applications. Based on their research, finned heatsinks could be a feasible solution for cooling from an economical perspective, if they are better at cooling than flat-plate heatsinks. However,

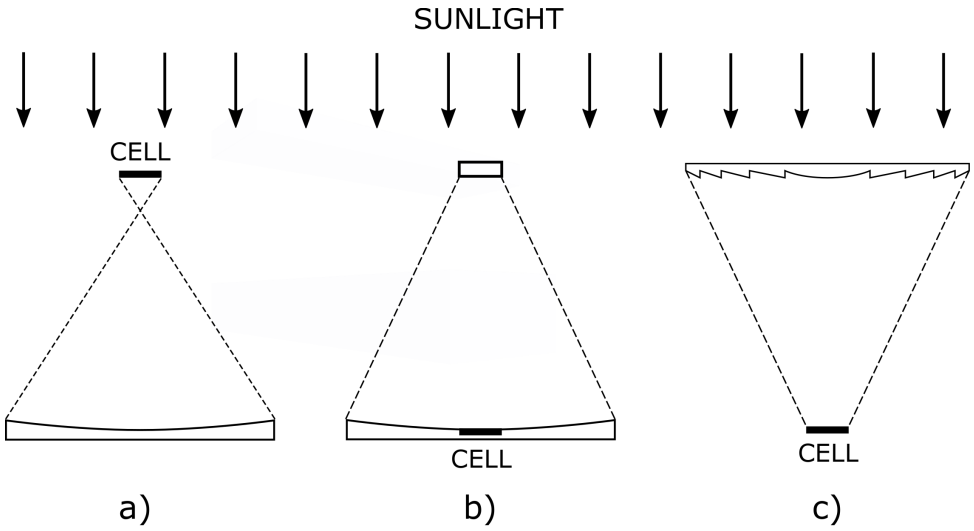

Figure 5.1 *Different concentrating optic configurations. In a) the available cooling area for the cell is small, or otherwise some of the irradiation is blocked. In b) and c) the whole area of the concentrating optics is available for cooling.*

the increase of the surface area increases the friction forces between the air and the heatsink, making finned heatsinks unsuitable for natural convective cooling [13, p. 415]. A simpler and more suitable design for passive cooling is a flat-plate heatsink. In this section we consider a 4 mm thick flat-plate aluminum heatsink, which has a good balance between the thermal performance, weight and the cost [39, 131]. For passive cooling, a concentrator with a Fresnel lens is considered (see Figure 5.1c). In this configuration the whole area of the concentrating lens is available for cooling purposes, therefore the heatsink dimensions were defined so that $A_{\text{heatsink}} = X \cdot A_{cell}$.

The convective heat transfer coefficients on heatsink surfaces are dependent on the characteristic length of the heatsink. As the concentration increases, the size (and the characteristic length) of the heatsink increases also. However, in practice the characteristic length of the system is not the characteristic length of an individual heatsink under a cell but rather that of a panel assembly. Thus, we consider the single cell package to be part of a bigger panel assembly with dimensions of $1.0 \times 1.5\,m^2$. It is reasonable to assume that the convective air flow over the upward facing surface of the cell, the Al_2O_3 substrate and the heatsink is similar to the airflow over the entire panel. Thus, the convective heat transfer coefficients over all upward and downward facing surfaces are based on the panel dimensions.

Two passive cooling scenarios are considered: First, in the low temperature scenario, the cell package in addition to the upward and downward facing surfaces of the heatsink are cooled by natural convection. In addition, all free surfaces emit heat by radiation. However, in practice the space between the cell and the concentrating

optics is closed to some extent. Therefore, the natural convection on upward facing surfaces is not ideal as the temperature of the air inside the panel is not the same as the ambient air temperature. Thus, in the second scenario we consider a high-temperature case, where cooling by natural convection is disabled on the upward facing surfaces. In this way we can find the extremes for the operating temperature of the cell. In addition, both high and low temperature scenarios were considered with varying emissivities on the downward facing surface of the heatsink: In the low emissivity case we used the emissivity of aluminium (ϵ=0.10, see Table 4.2) and in the high emissivity case the emissivity of a painted surface (ϵ=0.90) [48].

A passively cooled unit consisting of a 3C44 solar cell, an Al_2O_3 substrate and a heatsink was simulated under varying concentrations. In the simulation the cell is placed horizontally, and the convective heat transfer rates were calculated with horizontal plate approximations defined in Table 3.2. The simulation results are presented in Figure 5.3a. In practice, the CPV-panel is almost never at a 0° angle outside of the equatorial area, so it is reasonable to simulate the cooling conditions at an angle, which has effect on the heat transfer coefficients of natural convection. Thus, another simulation with varying angles was run at a constant concentration of 250 suns. The inclination angle varied between 30° and 90° (measured from the horizontal level), because the inclined plate approximations presented in Table 3.2 are valid only for $-60° < \theta < 60°$ (measured from the vertical level). The results are presented in Figure 5.3b.

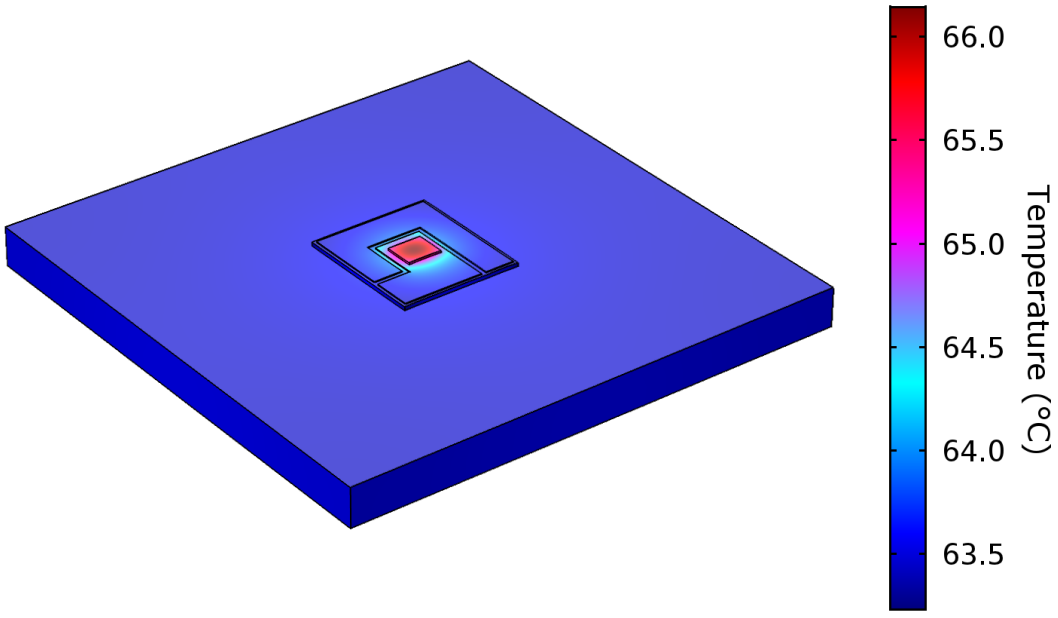

Figure 5.2 *The temperature profile of a passively cooled package on a flat-plate heatsink under a 250-sun concentration.*

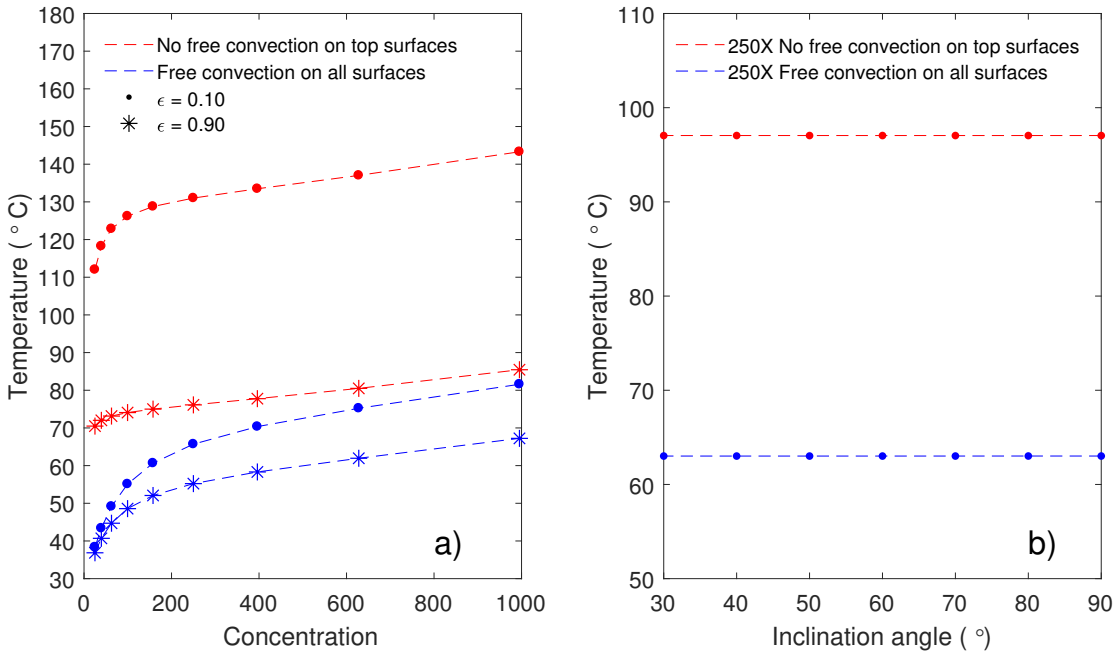

Figure 5.3 *Passive cooling under different concentrations. The temperature of the cell with free convection at all surfaces is presented in blue. The temperature of the cell when no natural convection occurs on upward facing surfaces is presented in red. a) Operating temperature as a function of concentration at a constant angle of 45°. The low emissivity case is marked with dots (•) and high emissivity case with asterisks (∗). b) The effect of the inclination angle on the operating temperature.*

The recommended maximum operating temperature for the 3C44 cell is 110 °C [6]. As seen in Figure 5.3a, in the low temperature scenario the temperature stays well below the recommended temperature regardless of the emissivity. In fact, between the high and low emissivity cases the temperature difference is less than 10 °C at concentrations below 250 suns, and 14.36 °C at 1000 suns. The influence of emissivity is thus relatively small, and the operating temperature is more dependent on the convective cooling. This is expected, as the emission power is dependent on the fourth power of the temperature difference. However, in the high temperature scenario, the operating temperature is above the recommended temperature at all simulated concentrations in the low emissivity case. Therefore, in the worst case scenario passive cooling is not sufficient. In the high emissivity case the temperature decreases significantly. This is again expected due to the temperature being dependent on the emission power. Surprisingly, the cell temperature in the high temperature scenario with high emissivity is almost independent of the concentration. This can be explained by the increasing surface size of the heatsink, as the emission power is proportional to the surface area. In addition, as the concentration increases, the cell temperature in the high temperature scenario with high emissivity approaches the temperatures of the low temperature scenario with low emissivity.

The angle of the CPV-panel seems to have no effect on the operating temperature, as seen in Figure 5.3. This is because the convective flow over the panel is turbulent: As the panel size increases, the Rayleigh number also increases. The Rayleigh number as a function of characteristic length is plotted in Figure 5.4. As we can see, at $L > 0.62$ m, $Ra > 10^9$ i.e. the fluid flow over the panel is turbulent. In this case the Nusselt number approximation for an inclined plate is not dependent on the angle, as seen in Table 3.2. Even though the values for the Nusselt number are only approximations, this needs to be taken into consideration when designing a passively cooled panel: as natural convective flow has no external driving force, it becomes easily turbulent as the characteristic length increases.

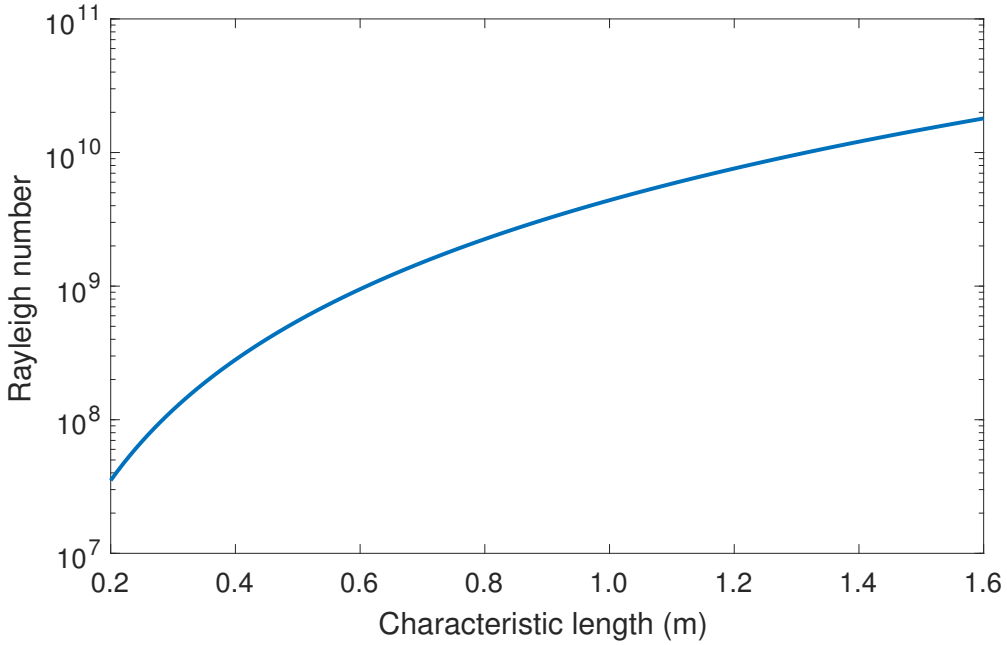

Figure 5.4 *Rayleigh number versus characteristic length. The line was plotted assuming surface temperature of 75 °C and ambient temperature of 25 °C*

The efficiency of the cell under different concentrations for the high and low temperature cases with high and low emissivities is evaluated in Figure 5.5. The efficiency of the cell peaks around 250-sun concentration (see Figure 4.4), which can be seen especially in the high temperature scenario in Figure 5.5. Beyond 250 suns the effect of increasing heat load (and as a consequence temperature) starts to influence the operating efficiency. In addition, the concentration dependency of the efficiency begins to limit the efficiency of the cell. In the high temperature scenario with low emissivity the operating efficiency of the cell drops to 37 %, whereas in the low temperature scenario with low emissivity the efficiency stays above 40.5 % even at 1000 suns. In the low temperature and high emissivity scenario the efficiency stays between 41–43%.

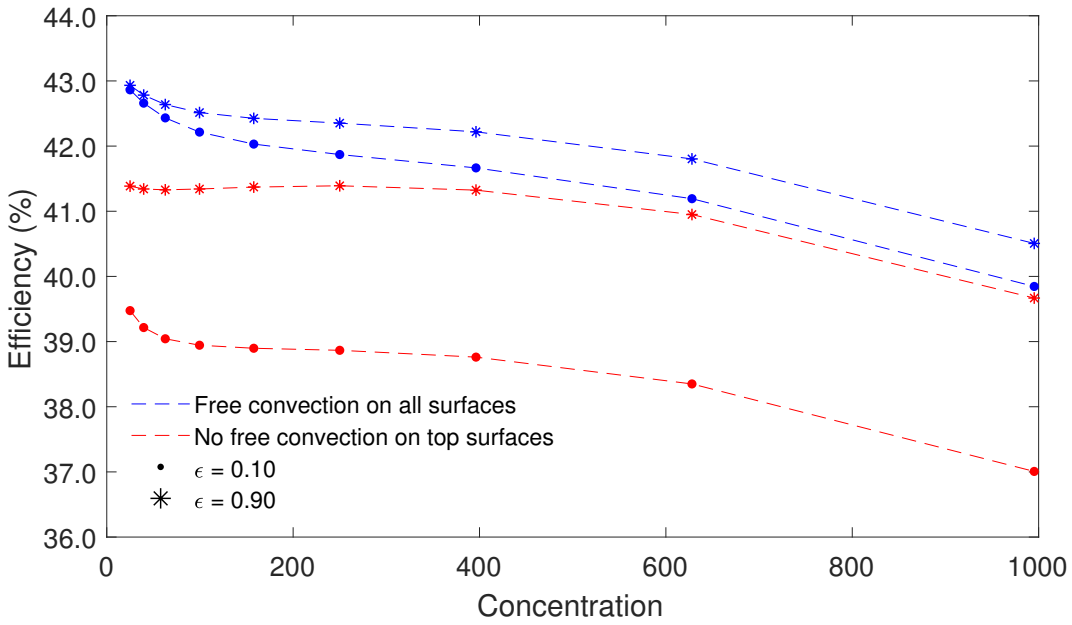

Figure 5.5 *Efficiency of the cell under different concentrations. The low temperature scenario is shown in blue and the high temperature scenario in red.*

5.2 Active cooling by forced convection

Compared to passive cooling, active cooling by e.g. wind should offer better heat transfer coefficients and thus lower operating temperatures due to higher fluid velocity. As wind is not always present, active cooling often requires external power for inducing the convection. To compensate the loss in system efficiency due to external cooling, the output power of the cell must increase more than what is required for the forced convection.

A 3C44 cell on a flat-plate aluminium heatsink was simulated under different wind velocities. The downward facing surface of the heatsink is cooled down by forced convection in all cases. Three convective cooling scenarios for upward facing surfaces were investigated: natural convection, no cooling by convection and forced convection with same wind velocities as the downward facing surface. The operating temperatures of the cell are presented in Figure 5.6.

The case with natural convection on upward facing surfaces is presented in Figure 5.6a. The wind velocity has minimal effect (<4.6 °C difference between 1 m/s and 5 m/s) at concentrations below 100 suns. As the concentration increases, the temperature difference between different wind velocities slightly increases. At 1000 suns the temperature difference between 1 m/s and 5 m/s wind velocities is 10.25 °C. The case with no convective heat transfer on upward facing surfaces is presented in Figure 5.6b. The temperature decreases significantly with higher wind veloci-

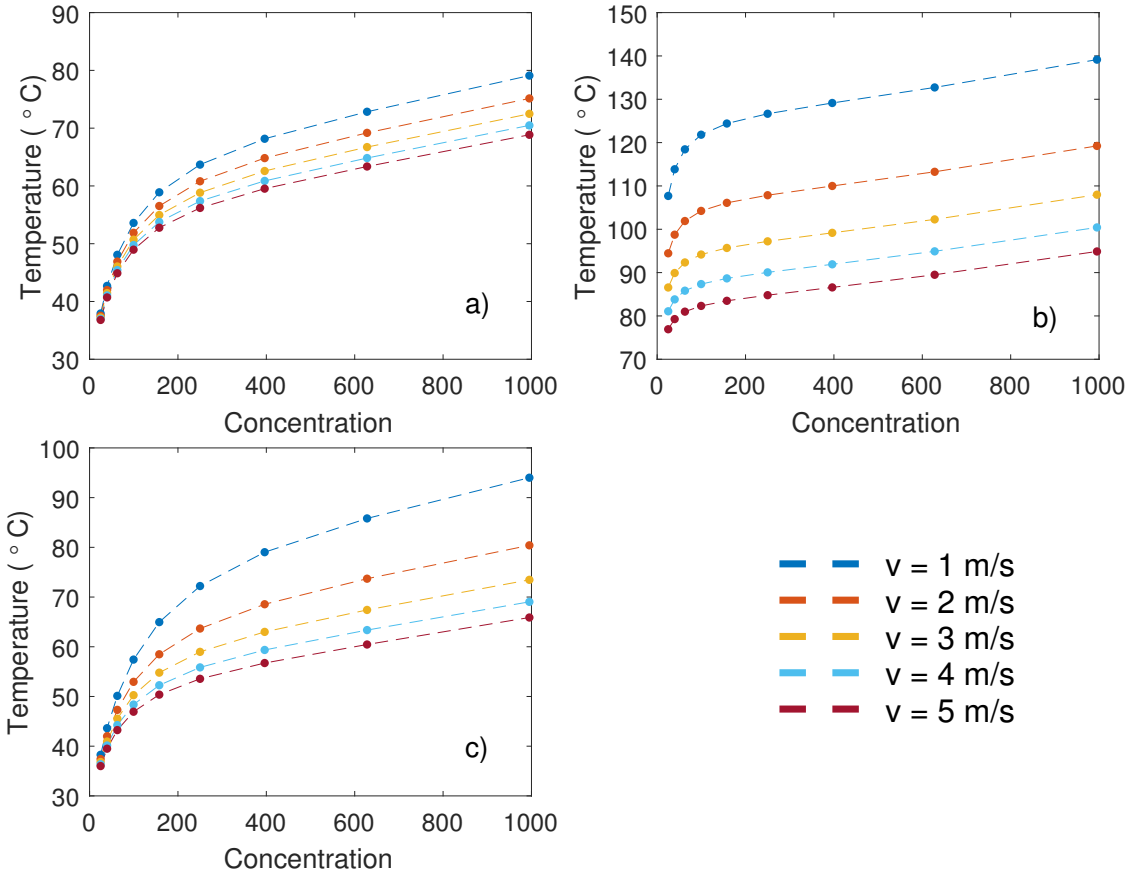

Figure 5.6 *External forced convection on the downward facing surface of a flat-plate heatsink with varying wind velocities under different concentrations. a) Natural convective cooling on upward facing surfaces. b) No convection on upward facing surfaces. c) Forced convection on upward facing surfaces.*

ties. This is expected, as the forced convection on the downward facing surface is the dominating cooling method. If the emissivity of the heatsink would be higher than the emissivity of aluminium (0.1), the operating temperature would be significantly lower even with low wind velocities, as we saw in Section 5.1. However, with $v \geq 3$ m/s the temperature stays below the recommended temperature of the cell. Even though the case with no convection on upward facing surfaces is the worst case scenario for forced convective cooling, reasonable operating temperatures can be reached. Lastly, the case with forced convection on both sides is presented in Figure 5.6c. Interestingly, the operating temperatures with wind velocities of v=1 m/s and v=2 m/s are higher than in the case with natural convection on upward facing surfaces (compare to Figure 5.6a). This indicates, that the heat transfer coefficients are greater with natural convection than with forced convection on the upward facing surface with wind velocities of $v \leq 2$ m/s. Somewhere between v=2–3 m/s the heat transfer coefficient of forced convection passes the heat transfer coefficient of natural convection. To investigate this, heat transfer coefficients (H) were evaluated

from the simulation model at the upward facing surface of the heatsink for all wind velocities and all concentrations. The heat transfer coefficients were then averaged over the concentration, as the values of H are more dependent on wind velocities rather than the concentration. The evaluation was done for two models: (i) wind on the downward facing surface and natural convection on the upward facing surface and (ii) wind on both upward and downward facing surfaces. The results are presented in Table 5.1.

Table 5.1 *Average heat transfer coefficients evaluated at the upward facing surface of the heatsink under different wind velocities.*

Wind velocity (m/s)	**H at upward facing surface for natural convection** $(W/(m^2 \cdot K))$	**H at upward facing surface for forced convection** $(W/(m^2 \cdot K))$
1	5.35	3.14
2	5.24	4.44
3	5.16	5.44
4	5.09	6.29
5	5.04	7.03

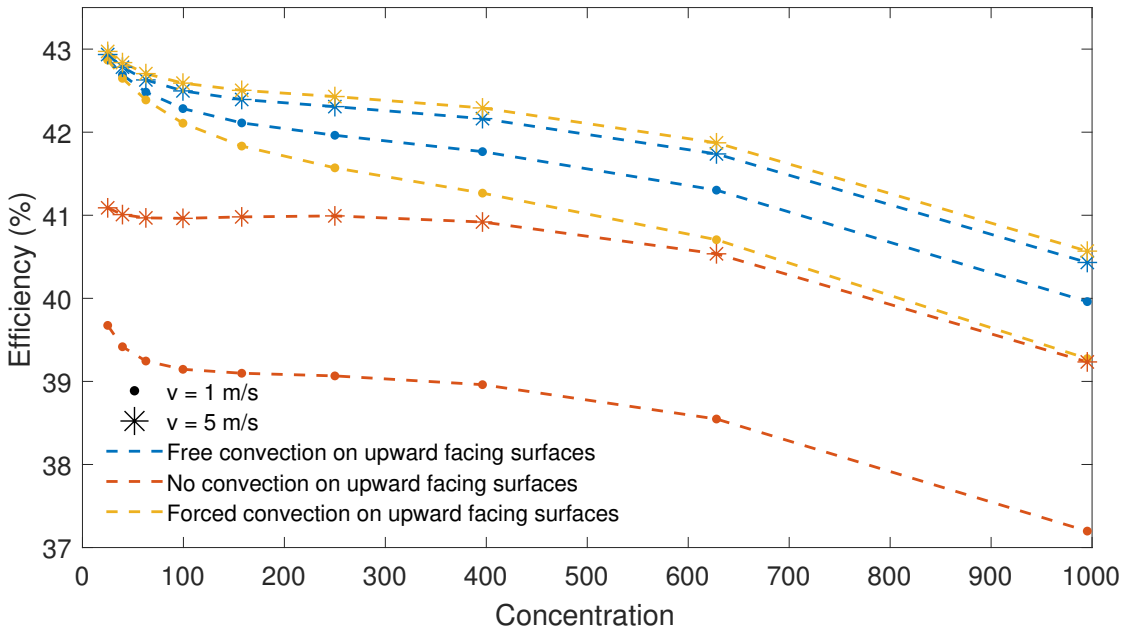

Figure 5.7 *Operating efficiency of the cell under different cooling schemes and wind velocities. In the figure there are only plotted efficiencies with wind velocities of v=1 m/s (•) and v=5 m/s (∗), to illustrate the extremes.*

The evaluation of heat transfer coefficients confirm that H is indeed higher with natural convection compared to forced convection, when $v \leq 2\,m/s$. This can be explained by the dragging force between the fluid and the surface: In natural convection, the fluid rises upwards from the surface, and the dragging force is minimal.

When the fluid flows along the surface, the friction forces between the fluid and the surface cause the wind velocity to drop in the boundary layer, resulting in lower heat transfer coefficients than with natural convection. As the wind velocity increases, H for the forced convection case surpasses H for natural convection. In contrary, for the natural convective case H is decreasing as a function of wind velocity. This is due to the decreased temperature of the upward facing surface for high wind velocities.

The operating efficiency of the cell under different cooling schemes and wind velocities is shown in Figure 5.7. The efficiency was evaluated only with wind velocities of v=1 m/s and v=5 m/s to illustrate the extremes. The behaviour of the heat transfer coefficients for natural convection and forced convection on the upward facing surface of the heatsink described earlier can be seen in Figure 5.7: Best efficiencies at v=1 m/s are reached with natural convection. However, as the wind velocity increases, the forced convective cooling on the upward facing surface starts to increase so that best efficiencies are reached with forced cooling at v=5 m/s.

5.3 Cell miniaturisation

In general, we can consider the thickness of the cell to be independent of the cell area, as CPV cells can be processed to varying sizes regardless of the wafer thickness. Thus, the ratio of the edge surface area to the top surface area is not constant if the cells edge length is varied. With smaller cells the edge surface area begins to dominate the total surface area. This effect is illustrated in Figure 5.8. As we can see, the edge surface area is equal to the top surface area at cell edge length of 0.76 mm. Cells smaller than this have more edge surface area than illuminated area. As the top surface area of the cell determines the concentration factor (if the size of the lens is fixed) and thus the heat input, the smaller the cell the more cooling area is available compared to the heat load.

To investigate the influence of the cell dimensions on the operating temperature, a simulation was run with varying cell sizes ranging from $0.3 \times 0.3\,mm^2$ to $9.49 \times 9.49\,mm^2$. The efficiency of the cell was considered to be independent of the cell dimensions. The packaging and the heatsink of the system were scaled in lateral dimensions with the size of the cell. However, the convective heat transfer coefficients are dependent on the characteristic length, which varies within varying cell sizes. To see the effect of the dominating edge surface area, we cannot vary the characteristic length of the cell package for convective cooling, because it would distort the results. Thus, we assume the cell to be part of a panel with dimensions of $1.0 \times 1.5\,m^2$. Upward facing surfaces of the cell and the heatsink and the downward

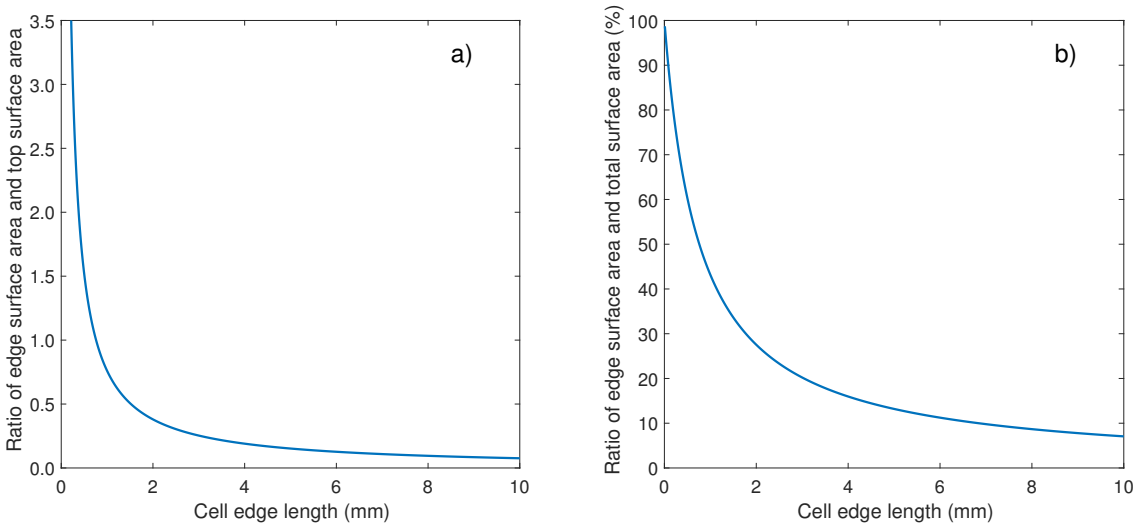

Figure 5.8 *a) The ratio of edge surface area and top surface area as a function of cell edge length at a constant cell thickness of 0.19 mm. b) The ratio of edge surface area and total area as a function of cell edge length. As the cell dimensions diminish, the edge surface area starts to dominate the total surface area.*

facing surface of the heatsink are cooled by natural convection described in Section 5.1. The characteristic length is defined by the panel. All free surfaces are considered diffuse emitters. Because the thickness of the package and the cell is constant, the characteristic lengths for convective heat transfer on the vertical side walls of the package and the cell do not change. Thus, the vertical side walls of the package cool down by convective heat transfer.

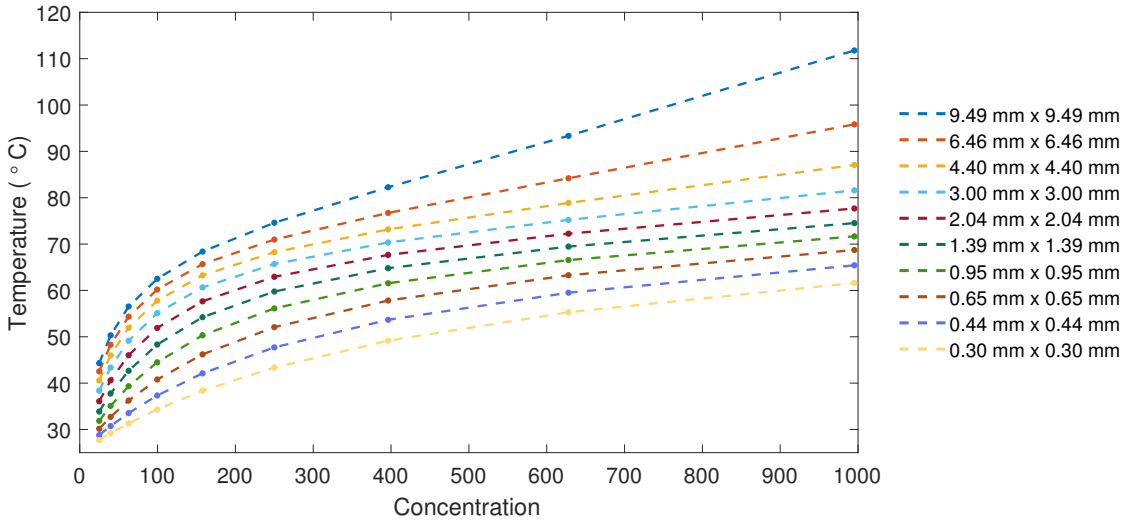

Figure 5.9 *The influence of the cell size on the operating temperature at various concentrations.*

The results of the simulation are presented in Figure 5.9. The operating temperature of the cell is clearly dependent on the cell size, as expected. The smallest cell operates

at the lowest temperature at all concentrations, whereas the biggest cell operates at the highest temperature. For reference, the cell with an edge length of 3.00 mm (light blue in Figure 5.9) is comparable to the results presented in Figure 5.3a. In addition, the temperature increases as a function of concentration for all cell sizes. However, this effect is greater with bigger cells, and would be even more visible if even bigger cells were considered in this simulation.

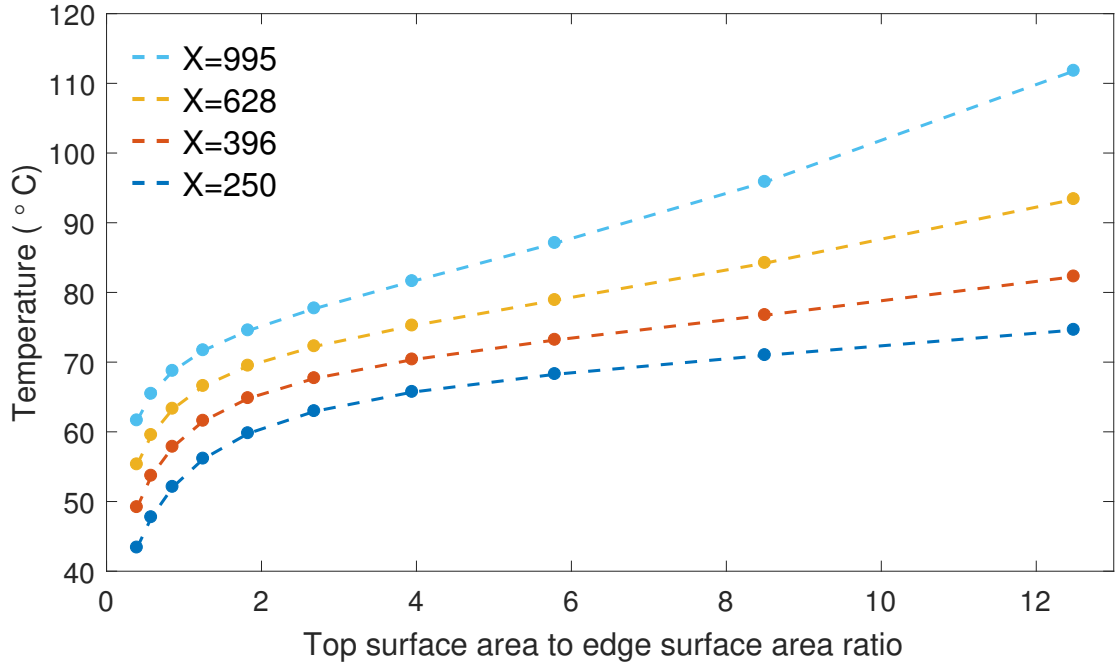

Figure 5.10 *Temperature of the cell as a function of the top surface area to edge surface area ratio.*

By selecting the temperature for all cell sizes at a fixed concentration from Figure 5.9, and by plotting them against the ratio of the top surface area to the edge surface area, we can investigate the influence of the cell size further. This is presented in Figure 5.10. The more top surface area there is compared to edge surface area, the hotter the operation temperature of the cell. This agrees with the predicted behaviour given in Figure 5.8. The temperature decreases rapidly below the ratio of 3. Above this, the top surface area starts to dominate the total area, and the operating temperature is clearly less dependent on the cell size.

5.4 Concentrated photovoltaics in space conditions

Convective heat transfer is not available in space conditions, as there is no air (nor any fluid) present. The heat is distributed via thermal conduction across the panel, but radiation is the only heat loss mechanism. Let's consider a 3C44 cell

bonded to a flat-plate aluminum heatsink in space. Even though the 3C44 cell is not optimized for AM0-spectrum, we will use it here to demonstrate the possibility of utilising concentrated photovoltaics in space by assuming similar performance with the AM0-spectrum as with the AM1.5D.

Let's first investigate the cooling scheme in space conditions for a CPV cell. In case of a Fresnel lens concentrating optics, the area of the lens is available for cooling purposes. The concentration ratio X can be thus expressed as

$$X = \frac{A_{lens}}{A_{cell}} = \frac{A_{heatsink}}{A_{cell}} \,. \tag{5.1}$$

The steady-state operating temperature of the cell is reached when the heat power is equal to the cooling power, i.e. $P_{in} = P_{out}$. The input energy is given by Equation 4.2 and the cooling power (by emission) per unit area is given by Equation 3.28. Thus, the steady-state power balance is

$$\eta_{opt} X I_{sun} A_{cell}(1 - \eta(X,T)) = \epsilon\sigma A_{heatsink}(T^4 - T_{amb}^4) \,. \tag{5.2}$$

Rearranging Equation 5.2 results in

$$T^4 = \frac{\eta_{opt} X I_{sun} A_{cell}(1 - \eta(X,T))}{\epsilon\sigma A_{heatsink}} + T_{amb}^4 \,. \tag{5.3}$$

Using Equation 5.1, we get

$$T^4 = \frac{\eta_{opt} X I_{sun}(1 - \eta(X,T))}{\epsilon\sigma X} + T_{amb}^4 \,. \tag{5.4}$$

Finally, the operating temperature is given by

$$T = \sqrt[4]{\frac{\eta_{opt} I_{sun}(1 - \eta(X,T))}{\epsilon\sigma} + T_{amb}^4} \,. \tag{5.5}$$

Thus, the operating temperature of the cell is almost independent of the concentration, as long as the dimensions of the heatsink are given by Equation 5.1. The efficiency is the only term dependent on the concentration, and this dependency is rather small. This independence from concentration is explained by examining the cooling equation: As the input power (i.e. concentration) increases, the cool-

ing power increases equally, as the concentration increases the size of the heatsink. However, it is important to note that this derivation was done by analysing only the power balance of the system. The dimensions of the system are not taken into account and no heat transfer occurs. In practice, the temperature is not independent of the concentration as there will be temperature differences caused by thermal resistances. On the other hand, this derivation demonstrates, that the smaller the thermal resistances of the panel assembly, the less the concentration has effect on the operating temperature.

To confirm the result of this derivation and to find a range of operating temperatures, a space-CPV system was simulated. The input energy is again given by Equation 4.2, where this time the intensity is the intensity of the AM0-spectrum (1366.1 W/m^2). As the cooling is solely based on radiative emission, the emissivity of the heatsink determines the operating temperature. In the simulation the emissivity of the heatsink is set to 0.9 on the downward facing surface, which is equal to the emissivity of a painted surface. In addition, the ambient background temperature is set to 3 K, which is equal to the background temperature of space, which increases the cooling power tremendously. Two scenarios with 3 K background temperature were simulated: a cell with a concentration dependent efficiency given by Equation 4.2, and a cell with a constant efficiency of 43%. The latter was simulated in order to see how much the concentration dependency of efficiency affects the temperature. In both cases, only the bottom surface of the flat-plate heatsink emits radiation to its surroundings. In addition, another simulation was done with the background temperature of 252 K, which is the effective temperature of the Earth. This simulates a situation, where the backside of the panel is facing Earth. This is the absolute worst case scenario for a CPV panel in space. The simulation results are presented in Figure 5.11.

The temperature of the cell stays below the recommended operating temperature for all cases, as is seen in Figure 5.11a. With η_{const} the temperature is linearly dependent on the concentration. Comparing it to the efficiency dependent on temperature and concentration $\eta(X, T)$, we can see a difference in slope and a difference in y-axis. The difference in y-axis is due to the linear temperature dependency of $\eta(X, T)$. The difference in slope is further explained by the concentration dependency of $\eta(X, T)$, which is quadratic as given by Equation 4.2. As expected, the concentration dependency of the efficiency is rather small. It can not solely explain the concentration dependency of the operating temperature, as the temperature is not independent of the concentration even with constant efficiency. This is due to a couple of reasons: First of all, the thermal resistance of the Al_2O_3 substrate, the solder and the thermal interface material create a temperature gradient between the

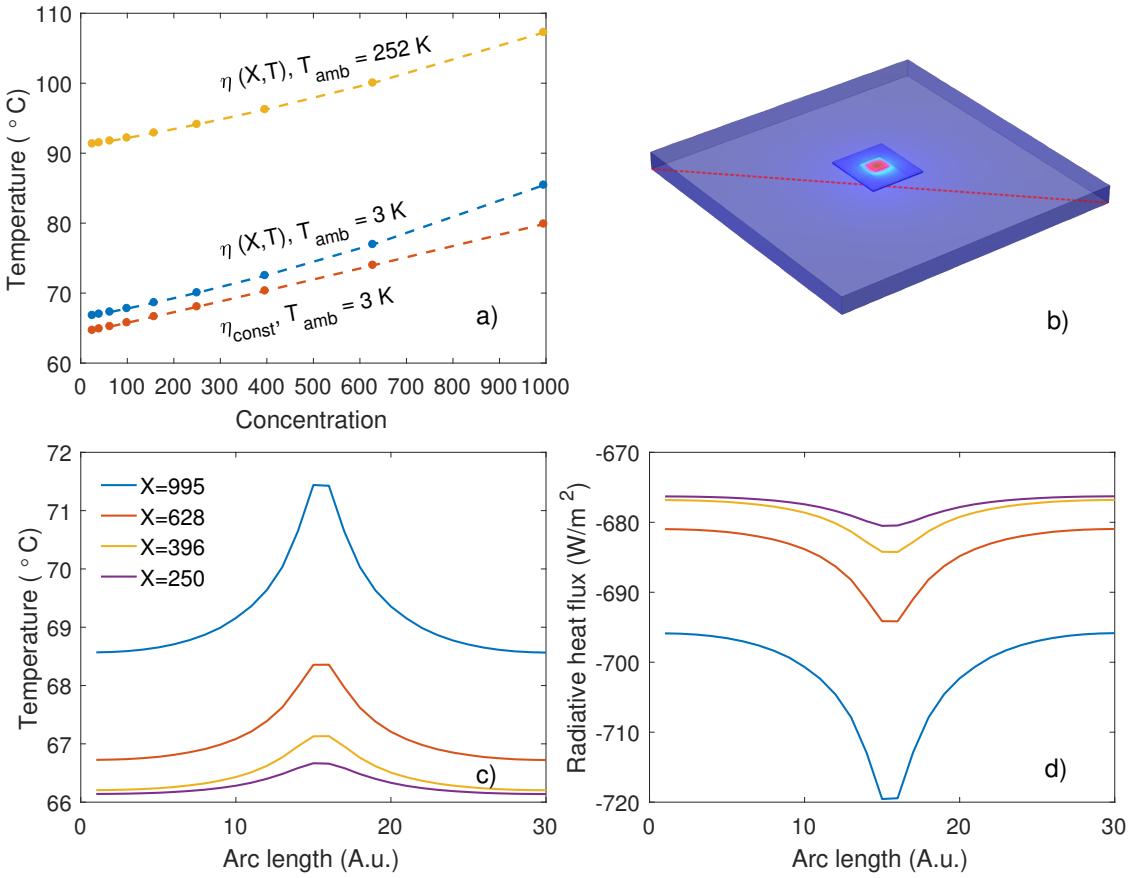

Figure 5.11 *Simulation results of a space CPV cell. a) The temperature as a function of concentration for two efficiency scenarios with 3 K background temperature and a scenario with background temperature of 252 K. b) The defined cut line from the bottom surface of the heatsink. c) The temperature profile along the cut line at various concentrations. d) The radiative heat flux profile along the cut line at various concentrations.*

cell and the heatsink. The temperature drop through the whole package from the top surface of the cell to the bottom surface of the heatsink is greater with higher input thermal fluxes, as indicated by Equation 3.3. This means that at high concentrations the heat produced by the cell is not conducted to the bottom surface of the heatsink as effectively as with low concentrations. If the cell were bonded directly to the heatsink, and by assuming perfect thermal contact, the temperature difference would only be 3 °C between concentrations of 100 and 1000 suns. In that case the operating temperature seems to be almost independent of concentration, as expected by Equation 5.5.

Secondly, the radiative heat flux from the bottom surface of the heatsink is dependent on the surface temperature, as indicated by Equation 3.26. As the size of the heatsink increases with an increase in concentration, there will be a greater temperature difference between the middle of the heatsink and the edge of the heatsink,

as shown by Figure 5.11c. Thus, the radiative heat flux is highest near the center of the heatsink, and it diminishes towards the edges. The bigger the heatsink, the bigger the heat flux intensity difference, as seen in Figure 5.11d. This is the sole reason that causes the temperature not be dependent on the concentration even though we could minimise the thermal resistance between the cell and the heatsink.

5.5 Sub-bandgap energy photon filtering

The photons below the lowest bandgap of the multi-junction solar cell cannot be used for photovoltaic conversion and are converted to heat when absorbed. One approach to reduce this unnecessary heat generation would be to filter these photons before they enter the solar cell. This could be achieved by an anti-reflective coating with high reflectance for sub-bandgap photons. This kind of approach has been already demonstrated for a GaAs solar cell by Beauchamp et. al. [9], with a highly reflective coating from 900 nm to 1600 nm. This wavelength range accounts for 228 W/m^2 in the AM1.5D spectrum and 345 W/m^2 in the AM0, which result in significant reduction in heat generation.

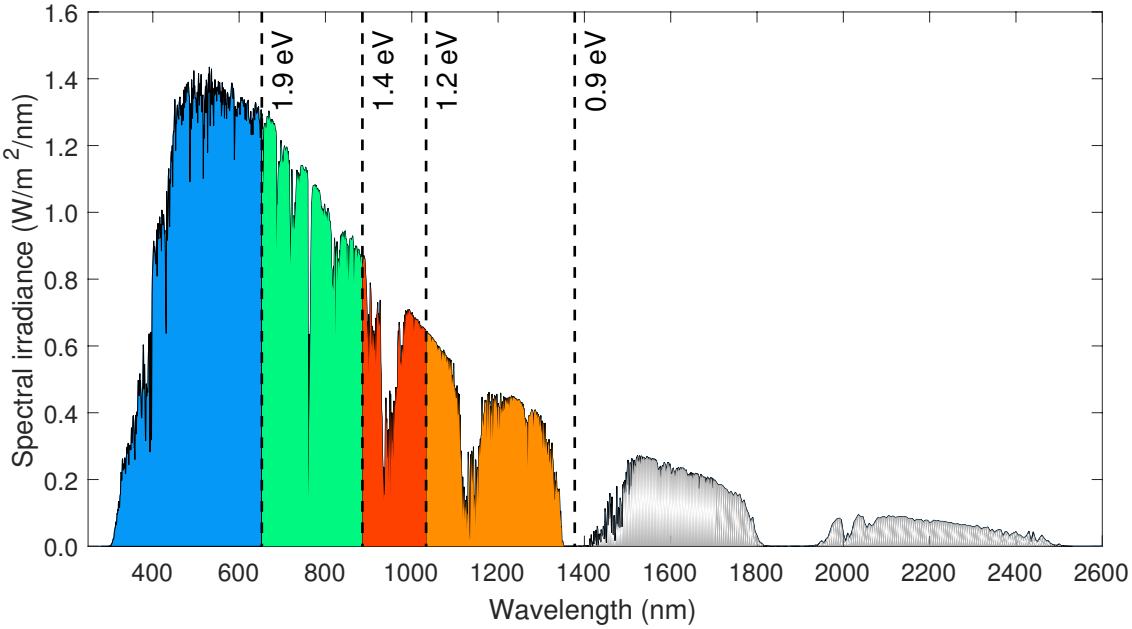

Figure 5.12 *Absorption of a 4J solar cell with bandgaps of 1.9, 1.4, 1.2 and 0.9 eV. The sub-bandgap photons are shown in grey.*

Let's consider a 4-junction (4J) solar cell with bandgaps of 1.9 eV, 1.4 eV, 1.2 eV and 0.9 eV (see Figure 5.12). All photons below the energy of 0.9 eV do not contribute to the photocurrent, and could be filtered before they enter the cell. The integrated irradiation energy for photons below 0.9 eV from the AM1.5D spectrum

is 107 $\mathrm{W/m^2}$, which accounts for 11.89% of the incident energy. However, because none of this irradiation is converted to electricity, most of it is converted to heat. Here we consider a case, where 100% of the out-band photons are absorbed by the substrate. For example, a cell operating at a 43% efficiency under AM1.5D absorbs 57% (513 $\mathrm{W/m^2}$) of the incident energy as heat. The sub-bandgap photons account for 20.8% of the total heating power. The in-band efficiency, i.e. the efficiency for photons above the lowest bandgap, is therefore 48.8% for the 4J solar cell presented here.

Let's consider a thermal model where the heat generation is lowered by sub-bandgap photon reflection. Here we denote the intensity of the photons with energy above the smallest bandgap as $I_{in-band}$ and the intensity of the sub-bandgap photons as $I_{out-band}$. If the anti-reflective coating has a reflectance R for the sub-bandgap photons, and A is the illuminated area, the heat generation in the cell can be formulated in the following way:

$$
\begin{aligned}
&I_{op} = 900\,\mathrm{W/m^2} && \eta = \tfrac{P_{out}}{I_{op}A} \\
&I_{out-band} = 107\,\mathrm{W/m^2} && \eta_{in-band} = \tfrac{P_{out}}{I_{in-band}A} \\
&I_{in-band} = 793\,\mathrm{W/m^2} && Q_{heat} = I_{in-band}\,A\,(1-\eta_{in-band}) + (1-R)I_{out-band}
\end{aligned}
$$

Thus, the heat load Q_{heat} is the sum of two components: the energy converted to heat from in-band photons that are not converted to electricity and the absorbed out-band photons not reflected by the anti-reflective coating. With this formulation we can calculate the heat load and operating efficiency for different values of R. For simplification we assume that on average the anti-reflective coating reflects 100R% of the sub-bandgap photons while the transmittance for higher energy photons is unity. We consider the cooling to be passive cooling presented in Section 5.1. In addition, a simulation without the reflector is used as a reference. For both models we incorporate a simple temperature dependency of the efficiency η:

$$\eta(T) = 0.43 - 0.0006\,\frac{1}{K}\,(T - 298.15\,\mathrm{K}). \tag{5.6}$$

This is based on Equation 4.2. However, here we consider a slightly higher temperature dependency of efficiency. This is due to an additional junction compared to the 3C44 cell. In addition, we have neglected the concentration dependency. The operating efficiency of the cell was then evaluated at different concentrations. The temperatures and efficiencies as a function of concentration are presented in Figure 5.13.

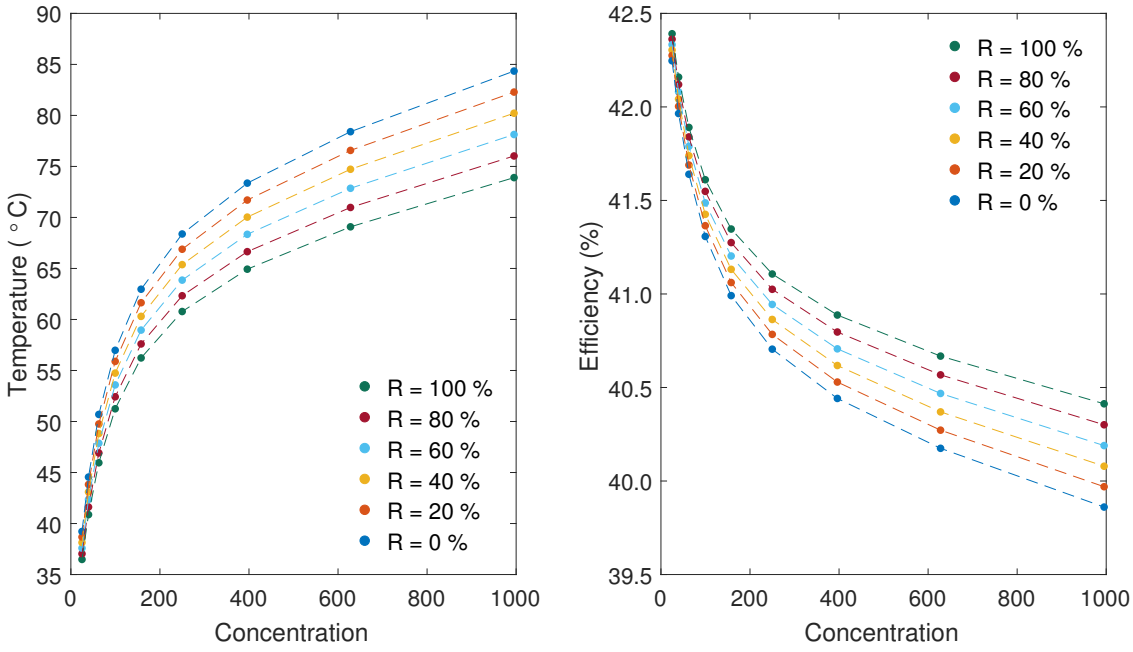

Figure 5.13 *Temperature and efficiency with different reflectors as a function of concentration. The line marked with dark blue dashes (R = 0%) is the reference case without the reflector.*

Reflecting the sub-bandgap photons before they enter the cell results in lower operating temperatures, as expected. In addition, because we have modelled the temperature dependency of the efficiency within the simulation, the effect of reducing the heat load is emphasized. A highly reflecting (R = 100%) mirror for sub-bandgap photons can lower the operating temperature of the cell by 10.45 °C at a concentration of 1000 suns. This results in a 0.55% improvement in efficiency.

6. ANALYSIS

In the first two sections of Chapter 5, two general cooling methods were investigated: passive cooling based on natural convection and active cooling based on forced convection. Compared to a passively cooled system with natural convection on all surfaces, lower temperatures were reached with natural convection on upward facing surfaces and forced convection on downward facing surfaces at all wind velocities. However, when the cooling on both upward and downward facing surfaces is forced, the passive cooling scenario reached lower operating temperatures with wind velocities $v \leq 1$ m/s. This is due to the observation that natural convective cooling can reach higher values for H over a flat plate with L=1.5 m compared to forced convection, as already discussed in Section 5.2. However, convective heat transfer relations presented in Table 3.2 are approximations, and in practice this might not be the case. In any case, at low wind velocities the convective heat transfer coefficient H for forced convection is probably very close to the H of natural convection.

A scenario where the upward facing surfaces were insulated from convection was studied for both passive and active cooling (see Figures 5.5a and 5.6b). Again, the case where v=1 m/s provides only slightly (5 °C) lower temperatures compared to the corresponding passively cooled scenario, which further indicates, that the forced convection with low wind velocities is rather close to the natural convection. However, at wind velocities ≥ 2 m/s the temperature is significantly lower for the active cooling. With increased surface emission, active cooling only on the downward facing surface of the heatsink could provide rather low (< 70 °C) operating temperatures for all concentrations up to 1000 suns. In practice, providing active cooling only on the downward facing surface of the heatsink could be a feasible solution, as the upward facing surfaces are in a more closed space, and adequate fluid flows might be hard to achieve.

The influence of emissivity was shortly studied in Section 5.1, where the emissivity of the downward facing surface of the heatsink was increased from 0.1 to 0.9 in the passive cooling scenario. The effect was very much the expected; if other cooling methods are sparse, emission can be really effective. As the emission power is depen-

dent on the differences of the fourth power of the surface and ambient temperatures (see Equation 3.28), it has impact on the cooling only if (i) the surface temperature is high compared to the ambient temperature, (ii) the ambient temperature is low compared to the surface temperature or (iii) the emissivity of the surface is high. In CPV, where the sun is tracked precisely, the surface behind the panel is definitely at a lower temperature compared to the back surface of the panel due to the shadowing of the panel. Thus in general, cooling by radiation is always present in the backside. In this thesis emission was also assumed on all upward facing surfaces except in the space CPV study presented in Section 5.4. However, heat conducts from the panel to the lens, as it is part of the structure. The upward facing surfaces do thus not emit black-body radiation to ambient temperature, but to the temperature of the lens. Therefore, the radiative heat exchange on the upward facing surfaces of the panel are probably overestimated. In reality, depending on the designed system, the temperature of the lens can be very close to the temperature of the cell, and only slight net heat exchange between the cell and the lens takes place. This could be simulated in COMSOL, as surface-to-surface radiation can also be studied. However, it requires a more complex model of a panel assembly than what was presented in this thesis. This kind of study could be conducted when designing a prototype of a panel. For the same reasons, radiative cooling was disabled from the top surfaces of the space CPV model presented in Section 5.4. A heatsink at 75 °C emits most of its energy in the wavelength range from 6 to 15 µm. In general, lens materials like PMMA and glass absorb effectively beyond the infra-red range [19, 28]. Therefore, even though the lens would be detached from the heatsink structure (i.e. the heat is not conducted to the lens), the lens would absorb the black-body radiation emitted by the cell and the heatsink. Eventually, the lens would almost reach the temperature of the cell. Thus, assuming a 3 K background temperature for the upward facing surface of the space CPV heatsink can not be justified.

Convective cooling (forced and natural) are both highly dependent on the characteristic length of the system. In Chapter 5 all cell packages were simulated as a part of a $1.0 \times 1.5\,m^2$ panel assembly to simulate operational CPV panels. As we saw in Section 5.1, the characteristic length was already big enough for the fluid flow to be turbulent on an inclined plate. The characteristic length should be less than 0.62 m for the flow to be laminar. This should be taken into consideration when designing a passively cooled CPV system. However, the angle of the plate had no influence on the heat transfer coefficients, since with a turbulent flow the angle dependency diminishes from the approximation of the Nusselt number. However, when comparing the inclined plate equations from sources [26, pp. 571–583], [14, pp. 257–258] and [13, pp. 418–419], it seems that the approximations for H on an inclined plate

can be interpreted in two ways. In COMSOL [14], which is based on source [26], the value of H is not dependent on the angle if the flow of the fluid is turbulent. However, from source [13] it can be understood, that the cosine should be included in the calculation of the Grashof number (i.e. g should be replaced by $g\,cos\,\theta$ in Equation 3.9), rather than inserting it into the equation for the Nusselt number. If the angle is taken into account when calculating the Grashof number, the characteristic length where the flow turns into turbulent is dependent on the angle. In addition, the Nusselt number approximation for the turbulent flow is dependent on Rayleigh number, which in turn has dependency on the Grashof number. Therefore, the angle would effect the flow in an inclined plate even when the flow is turbulent.

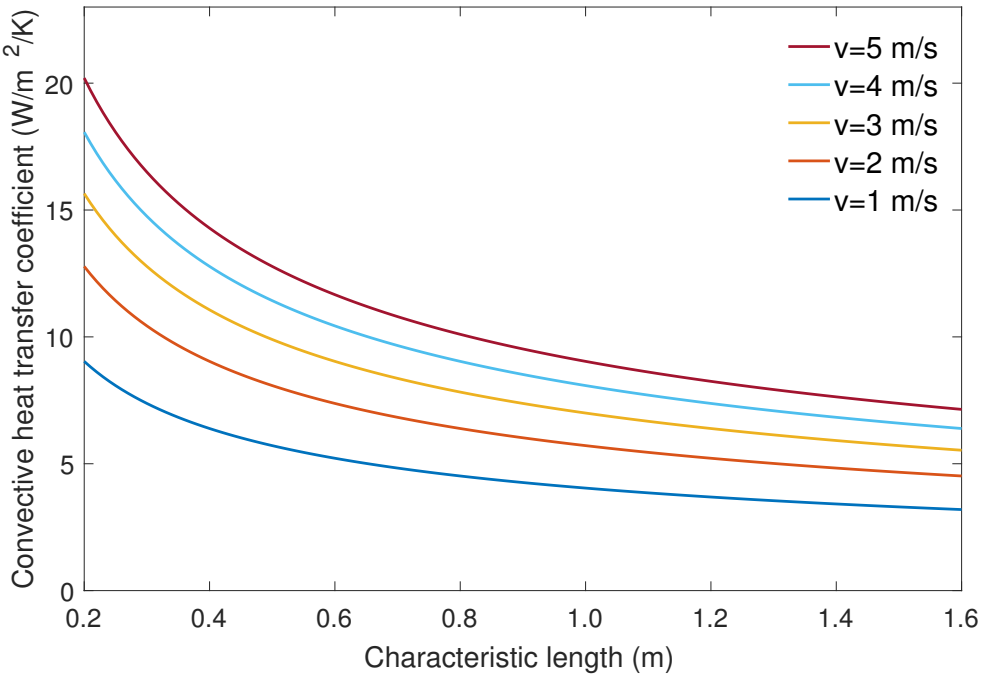

Figure 6.1 *Convective heat transfer coefficients as a function of characteristic length under varying wind velocities.*

In the forced cooling scenario, the plate length also has influence on the heat transfer coefficients of the system. Values of H are plotted as a function of characteristic length under varying wind velocities in Figure 6.1. The calculations were done assuming a surface temperature of 75 °C using equations presented in Section 3.2. As we can see, the heat transfer coefficients decrease rapidly as L increases from 0.2 m to 0.8 m. With L>0.8 m, the influence of the increasing characteristic length starts to saturate. This is yet again an important thing to keep in mind when designing an actively cooled panel.

As mentioned in Section 5.2, active cooling can be justified if more output power can be gained by lower operating temperatures than it requires power for cooling.

Table 6.1 *Evaluated output power for a single cell and a panel for the high-temperature passive cooling scheme.*

X (suns)	η (%)	P_{out} for a single cell (W)	# of cells in a $1.0 \times 1.5\,m^2$ area	P_{out} for a panel (W)
25	39.48	0.091	5530	503.31
40	39.22	0.143	3489	499.99
63	39.04	0.226	2202	497.80
100	38.94	0.357	1389	496.54
158	38.90	0.566	876	495.94
250	38.87	0.896	553	495.54
396	38.76	1.416	349	494.20
628	38.35	2.221	220	488.96
995	37.01	3.397	139	471.84

This is of course invalid if the thermal energy of the coolant is utilised. However, such case is not considered here. With natural convection on all surfaces of the cell, the operating temperatures were only slightly higher than for the cell with natural convection on the upward facing surface and forced cooling applied on the downward facing surface. Therefore, in this case active cooling cannot be justified, as the gain in output power is not very significant. However, as discussed previously, passive cooling based on natural convection might underestimate the temperature for two reasons: (i) there is no convection on the upward facing surface due to a closed space and (ii) the upward facing surfaces do not emit radiation to the ambient temperature but rather to the panel temperature. Therefore, the worst case scenario is that most of the heat is transferred away only from the downward facing surface of the heatsink. Let's consider the worst case scenario for both passive and active cooling. The efficiencies shown in Figure 5.5 are evaluated in Table 6.1 for various concentrations. The total output power for a $1.0 \times 1.5\,m^2$ panel was calculated based on the efficiency, the panel area and the optical efficiency. In addition, the output of a single cell was evaluated and the number of cells that would be needed to cover the panel area with their respective heatsinks and lenses were calculated for illustration purposes. For comparison, output powers were also evaluated for a panel, where the downward facing surface is cooled down by forced convection. The output power difference between a passively and actively cooled panel was evaluated, which gives us the amount of power available for a cooling system. The results are shown in Table 6.2. As we can see, the output powers of the actively cooled panels are 15 to 30 watts higher compared to the passively cooled panel. The difference increases as a function of concentration and wind velocity. This demonstrates the influence the active cooling has for a flat-plate panel. The effect would be even greater for a finned heatsink, where lower operating temperatures could be reached and therefore more output power could be gained.

Table 6.2 *Evaluated panel output powers for forced convection on the downward facing surface of the heatsink with different wind velocities. The ΔP_{out} is the difference in the output power of the panel with forced convection and the panel with passive cooling presented in Table 6.1.*

	v = 3 m/s			**v = 4 m/s**			**v = 5 m/s**		
X (suns)	η **(%)**	P_{out} **(W)**	ΔP_{out} **(W)**	η **(%)**	P_{out} **(W)**	ΔP_{out} **(W)**	η **(%)**	P_{out} **(W)**	ΔP_{out} **(W)**
25	40.65	518.24	14.93	40.90	521.46	18.16	41.09	523.88	20.58
40	40.52	516.62	16.63	40.80	520.19	20.20	41.01	522.85	22.86
63	40.45	515.69	17.89	40.75	519.51	21.71	40.97	522.34	24.54
100	40.42	515.32	18.78	40.73	519.32	22.78	40.96	522.28	25.74
158	40.42	515.34	19.41	40.74	519.46	23.52	40.98	522.50	26.56
250	40.42	515.37	19.83	40.75	519.56	24.02	40.99	522.65	27.11
396	40.34	514.32	20.12	40.67	518.58	24.38	40.92	521.72	27.51
628	39.95	509.34	20.37	40.29	513.66	24.70	40.54	516.83	27.87
995	38.63	492.56	20.72	38.98	496.98	25.14	39.23	500.23	28.39

However, in practice we cannot only evaluate the difference in the output power of the panel, as there are other remarks to be valued. First of all, the lower the operating temperature of the cell, the longer the lifetime of the panel [35]. Secondly, one must consider the initial investment of the panel versus the repayment time of the panel. If the investment spent on cooling cannot repay itself during the lifetime of the panel, the investment is obviously not worth it. However, in this thesis only a simplified case is considered, where the warm outlet fluid is wasted and not collected and utilised. Utilising the temperature of the coolant air would increase the total efficiency of the panel, but it would also increase the investment costs. The model presented in this thesis could be extended for evaluating the amount of heat that could be extracted from the panel.

Passive cooling for CPV has been studied earlier with COMSOL simulations. Micheli et. al. [32] have studied a passive cooling scheme for a flat-plate heatsink made of aluminium. The boundary conditions were similar to what was presented in Section 5.1: the cell is cooled passively by natural convection and radiation. However, there are some differences compared to this thesis. The intensity normalisation is different (900 W/m^2), the ambient temperature is 20 °C and the efficiency of the cell is constant. In their studies, the cell reached an operating temperature of 55 °C at a concentration of 1000 suns, which is significantly lower than what was found in Section 5.1. In addition, the concentration dependency of the temperature is linear. The relative difference in the operating temperature could be explained to some extent by a different ambient temperature and intensity normalisation, but the linear dependency can not. First of all, this is partly explained by the constant efficiency of the cell in the simulation. As the efficiency is evaluated at each simulation step,

its temperature dependency decreases more with higher concentrations. In addition, their selection of characteristic length for convective cooling is different, which can be interpreted from the article; they have simulated only a single unit consisting of the cell, Al_2O_3 substrate and a heatsink, with a characteristic length given by the heatsink and cell dimensions. This results in higher convective heat transfer coefficients, which explains the lower temperatures. Due to reasons discussed previously, using the length of a single unit as the characteristic length is a very optimistic approach to modelling passive cooling.

The influence of cell miniaturisation was only studied from the operating temperature point of view in Section 5.3. We found that miniaturisation of the cell decreased the operating temperature. In the simulations the efficiency was considered to be independent of the cell size, which is not quite true in practice. One of the most common loss mechanisms of solar cells is surface recombination, which is seen as a loss in voltage. In a simplified case, surface recombination can be divided to top surface recombination and edge surface recombination. Ultimately the voltage of the cell is dependent on the logarithmic ratio of the optically generated current I_{op} and the dark saturation current I_0, as seen in Equation 2.4. In essence, the dark saturation current is the total recombination current in the cell, i.e. in our case $I_0 = I_{0,top} + I_{0,edge}$, where $I_{0,top}$ is the current lost due to the top surface recombination and $I_{0,edge}$ is the current lost due to the edge surface recombination. Assuming no other recombination methods, we can rewrite the equation for V_{oc} as

$$V_{oc} \approx \frac{nk_bT}{q} ln\left(\frac{I_{op}}{I_{0,top} + I_{0,edge}}\right) \tag{6.1}$$

As solar cells are manufactured atomic layer by atomic layer from bottom to top, the top surface of the cell can be designed in such a way, that the top surface recombination can be minimised. However, the edge surface recombination is often problematic, as not much can be done to it when growing the cell. The edge surface recombination could be decreased with e.g. chemical treatments while processing the cell, but in most cases it would still exist. From Equation 6.1 we can see, that if $I_{0,top}$ is minimal, then the V_{oc} is dependent on the ratio of I_{op} and $I_{0,edge}$. The optically generated current depends on the top surface area, whereas the edge surface recombination depends on the edge length. Therefore, the smaller the cell the more there is edge surface area compared to the illuminated area (see Figure 5.8) and the smaller the ratio $\frac{I_{op}}{I_{0,edge}}$ becomes. Thus, miniaturisation decreases the operating voltage of the cell, diminishing the total efficiency. This was not taken into account in the simulations, and is something that could be investigated further. Miniaturisation

of the cells has other downsides too. Smaller cells might be more expensive to manufacture due to higher precision needed for processing and assembly. Especially the assembly of the optics must be very precise, because for very small cells (edge length $\leq$1 mm) only a slight misalignment results in a significantly reduced current. In addition, if the cells are separated from the wafer by sawing instead of dicing, the smaller the cell, the more cell material will be wasted. However, in smaller cells the electrical path is shorter compared to bigger cells, which results in smaller ohmic losses. This improves the efficiency of the cell and allows the cell to perform better at higher concentrations.

Radiative cooling in space conditions can be really effective, as was shown in Section 5.4. The extremes for the background temperature were studied, where in best case scenario the backside of the panel is pointing towards outer space with temperature of 3 K. In the worst case scenario the panel is facing towards the Earth with temperature of 252 K. Despite the huge difference (249 K) between the surrounding temperatures between these two scenarios, the operating temperatures were rather close to each other (22-25 °C difference for all concentrations). This is yet again explained by the nature of emission power; even though the background temperature is high, as the heatsink temperature increases, its emission power increases with the fourth power of the temperature. Therefore, a thermal equilibrium is reached below temperature of 110 °C under concentration of 1000 suns. III–V multi-junction solar cells are the best candidate for space photovoltaics due to their irradiation hardness and high efficiency. Based on this study, the operating temperature of the CPV cell is not the limiting factor for utilising CPV in space applications either. Therefore, problems arise from other aspects: The panel must withstand the transportation to space without altering the precise alignment of the cell and the lens. In addition, this requires the satellite to follow the location of the sun precisely. Also, a CPV panel, which requires more structural support compared to conventional solar panels, may weigh more. This increases the cost for the transportation. For the alignment problem one solution could be the use of low-concentration systems with high acceptance angle. Such concentrators for terrestrial applications have already been proposed by K. Araki et. al. [5]. In addition, thin-film solar cells could be utilised for reducing the weight of the panel.

Finally, sub-bandgap photon filtering for the cell presented in Section 5.5 showed improved operating temperatures and thus better operating efficiencies compared to the non-filtered case, as was expected. However, this filtering is only applicable for cells that do not fully utilise the whole spectral range of the sun. For example, below photon energy of 0.9 eV there is still 107 W/m^2, which accounts for 11.89% of the total integrated intensity of the sun. However, below 0.67 eV, which is the last dip

in the AM1.5D spectrum, there is only 31.84 W/m^2 left, which accounts for 3.54% of the total intensity. Thus, possible downsides from the optical filtering are bigger than the upsides of reflecting such small amount of energy. An important thing to note is, that the better the in-band efficiency of the cell, the more gain is achieved with sub-bandgap photon filtering. In this thesis the total efficiency of the cell was set to 43%, corresponding to 48.8% in in-band efficiency. In theory, the cell presented in Section 5.5 can reach an efficiency of 46.0%, which would result in an in-band efficiency of 52.2%. In addition, the efficiency of the cell had only dependency on temperature. If concentration dependency was included to the model, the benefit gained from sub-bandgap filtering would be even higher. However, such optical filters can be demanding to design and implement. In practice, high reflectance for photons below 0.9 eV means that we will see high reflectance for high-energy photons too. This will result in a reduced current in the top cell, and can further cause current-matching problems. Instead of reflecting the sub-bandgap photons before they enter the solar cell, they could be reflected at the bottom of the cell. In practice, this could be achieved by thinning the substrate of the cell and by depositing a highly reflective mirror (e.g. silver film) at the bottom. Effectively this would double the absorption length of the photons above the lowest bandgap, increasing the absorption efficiency. This has already been demonstrated by T. Aho et.al. [3]. However, this also doubles the absorption for the sub-bandgap photons in the structure. As a result, only part of the sub-bandgap photons would be reflected away. Thus, a highly reflective mirror before the cell could be a more feasible solution.

7. CONCLUSIONS

The main focus of this thesis was to construct a thermal model to study different cooling schemes for concentrated photovoltaics. This was done by establishing a COMSOL model of a single CPV cell attached to an Al_2O_3 substrate. The cell chosen for this study is a commercially available 3C44 Concentrator Triple Junction Solar Cell manufactured by AZUR SPACE Solar Power GmbH. The temperature and concentration dependency of the efficiency of the cell are known very well, which makes the cell suitable for the simulations presented in this thesis. A simple model of the cell efficiency as a function of concentration and temperature was formulated. By incorporating the temperature and concentration dependency in the simulation model, we were able to investigate the results that follow from the cycle where the temperature affects the efficiency and the efficiency affects the temperature. In steady-state simulations we can evaluate the efficiency of the cell afterwards, which gives us valuable numerical information about the power produced by the cell and the panel.

The simulation model used in this thesis was first validated by comparing it to measurements done in the laboratory. The most problematic aspect of simulating the measurement setup was the unknown (and relatively poor) thermal contact between the copper heatsink and the thermoelectric cooled steel heatsink. This was solved by modelling the thermal contact with a Cooper-Mikic-Yovanovich correlation. Another challenge was to initially define the time points when the V_{ocd} and V_{oc} were measured. Only a slight (0.02 s) error between the actual time point for the V_{ocd} measurement and the time point for temperature evaluation from the simulation model makes it impossible to fit the model with the measurements. However, with the selected boundary conditions, time points and materials, the simulations agreed very well with the measured values. As the validation in this thesis was done using a time-dependent simulation, steady-state measurements and simulations could be done to further validate the simulation model. However, if the thermal contact in the current solar simulator setup is not improved, the cell might break due to heat overload during steady-state measurements.

Different cooling methods were then investigated using the validated simulation

model as a base model. First, active and passive cooling schemes were studied. Both cooling methods proved to be sufficient to keep the cell below the recommended operating temperature. In the worst case scenario of passive cooling, where natural convection cools down the downward facing surface only, the operating temperature rose above the recommended temperature. However, it was shown that this could be compensated by increasing the emissivity of the downward facing surface. Active cooling lowered the operating temperature as expected. The total power gained from the lower operating temperature compared to the passive cooling scenario was evaluated, and the output power of a 1.0×1.5 m^2 panel with a concentration ratio of 995 rose by 20.72 W, 25.14 W and 28.39 W for wind velocities of v=3 m/s, v=4 m/s and v=5 m/s, respectively.

Cell miniaturisation also had clear effect on the operating temperature of the cell. Smaller cells cooled down more efficiently, which was seen as lower operating temperatures. However, the efficiency of the cell was considered to be constant for all cell sizes. For further investigation, a mathematical model needs to be established for estimating the possible loss that follows from diminishing the cell dimensions. There is a certain cell size, where the heat spreading, current spreading and edge surface recombination balance each other optimally, and maximum efficiency is achieved. Finding this would require accurate models for all three aspects.

Concentrated photovoltaics in space conditions showed promising results from the operating temperature point of view: the cell operated below the recommended operating temperature even in the worst case scenario, where the backside of the panel faced the Earth. Therefore, applying CPV in space is not limited by the operating temperature—problems arise from other challenges related to transportation, alignment and tracking.

The influence of sub-bandgap filtering on the operating temperature of a 4J solar cell was demonstrated. The operating temperature was clearly affected by the lowered heat input, as expected. The simulation assumed that the filter would not affect the current balance of the cell. In practice, this would be hard to achieve. Designing a sub-bandgap photon filter on glass and testing it with the 4J cell presented in this thesis could be considered as future work to investigate deeper into the subject. If this proves to be an impossible task, processing a back reflector to the cell would also be a feasible approach.

The thermal model developed in this thesis proved to be a useful tool in investigating different cooling scenarios. The results are in good agreement with the validation data gained from measurements and also agree with the predicted behaviour based

on theory. The performance of individual cells and the whole panel can be evaluated from the model with different cooling systems. Therefore, we can for example determine the payback periods for the capital invested in these systems. Now that the model is established, several parameters that were not studied in this thesis, could also be studied. The model can be used to vary e.g. materials, their properties, cell and packaging geometries or boundary conditions such as the ambient temperature. Previous paragraphs already suggested several improvements for modelling the cooling scenarios presented in this thesis. The geometry of the model could be further expanded to cover the geometry of an actual panel. In this way, other aspects such as surface-to-surface radiation could be incorporated into the model to gain more accurate results.

BIBLIOGRAPHY

[1] R. Adib, H. Murdock, F. Appavou, A. Brown, B. Epp, A. Leidreiter, C. Lins, H. Murdock, E. Musolino, K. Petrichenko *et al.*, "Renewables 2016 global status report," *Global Status Report RENEWABLE ENERGY POLICY NETWORK FOR THE 21st CENTURY (REN21)*, p. 272, 2016.

[2] A. Aho, "Dilute nitride multijunction solar cells grown by molecular beam epitaxy," Ph.D. dissertation, November 2015.

[3] T. Aho, M. Guina, F. Elsehrawy, F. Cappelluti, M. Raappana, A. Tukiainen, A. B. M. K. Alam, I. Vartiainen, M. Kuittinen, and T. Niemi, "Comparison of metal/polymer back reflectors with half-sphere, blazed, and pyramid gratings for light trapping in III—V solar cells," *Opt. Express*, vol. 26, no. 6, pp. A331–A340, Mar 2018. [Online]. Available: http://www.opticsexpress.org/abstract.cfm?URI=oe-26-6-A331

[4] A. Akisawa, M. Hiramatsu, and K. Ozaki, "Design of dome-shaped non-imaging fresnel lenses taking chromatic aberration into account," *Solar Energy*, vol. 86, no. 3, pp. 877 – 885, 2012. [Online]. Available: http://www.sciencedirect.com/science/article/pii/S0038092X11004580

[5] K. Araki, Y. Ota, K. Ikeda, K. H. Lee, K. Nishioka, and M. Yamaguchi, "Possibility of CPV for automobile energy source," in *2016 IEEE 43rd Photovoltaic Specialists Conference (PVSC)*, June 2016, pp. 0554–0559.

[6] *3C44 Concentrator Triple Junction Solar Cell Data Sheet*, AZUR SPACE Solar Power GmbH, 2015. [Online]. Available: http://www.azurspace.com/images/products/0004357-00-01_3C44_AzurDesign_3x3.pdf

[7] *Enhanced Fresnel Assembly Data Sheet*, AZUR SPACE Solar Power GmbH, 2015.

[8] A. Bar-Cohen, M. Iyengar, and A. D. Kraus, "Design of optimum plate-fin natural convective heat sinks," *Journal of Electronic Packaging*, vol. 125, no. 2, pp. 208–216, Jun 2003. [Online]. Available: http://dx.doi.org/10.1115/1.1568361

[9] W. T. Beauchamp, T. T. Hart, and M. L. Sanders, "Blue/red reflecting solar cell covers for GaAs cells," in *Conference Record of the Twenty Third IEEE Photovoltaic Specialists Conference - 1993 (Cat. No.93CH3283-9)*, May 1993, pp. 1487–1490.

[10] P. Benítez, J. C. M. nano, P. Zamora, R. Mohedano, A. Cvetkovic, M. Buljan, J. Chaves, and M. Hernández, "High performance fresnel-based photovoltaic concentrator," *Opt. Express*, vol. 18, no. S1, pp. A25–A40, Apr 2010. [Online]. Available: http://www.opticsexpress.org/abstract.cfm?URI=oe-18-101-A25

[11] BP, "Statistical review of world energy 2016." [Online]. Available: https://www.bp.com/content/dam/bp/pdf/energy-economics/statistical-review-2016/bp-statistical-review-of-world-energy-2016-full-report.pdf

[12] S. Brenner and L. Scott, *The Mathematical Theory of Finite Element Methods*, ser. Texts in Applied Mathematics. Springer New York, 2013.

[13] Y. Çengel, *Heat transfer: a practical approach*, ser. Schaum's outline series in mechanical engineering. WBC McGraw-Hill, 1998.

[14] COMSOL, *Heat Transfer Module User's Guide*.

[15] ——. Multiphysics cyclopedia: The finite element method (FEM). Accessed: 25.3.2018. [Online]. Available: https://www.comsol.com/multiphysics/finite-element-method

[16] M. Cooper, B. Mikic, and M. Yovanovich, "Thermal contact conductance," *International Journal of heat and mass transfer*, vol. 12, no. 3, pp. 279–300, 1969.

[17] O. Dupré, R. Vaillon, and M. Green, *Thermal Behavior of Photovoltaic Devices: Physics and Engineering*. Springer International Publishing, 2016.

[18] N. J. Ekins-Daukes, P. Sandwell, J. Nelson, A. D. Johnson, G. Duggan, and E. Herniak, "What does CPV need to achieve in order to succeed?" *AIP Conference Proceedings*, vol. 1766, no. 1, p. 020004, 2016. [Online]. Available: http://aip.scitation.org/doi/abs/10.1063/1.4962072

[19] Y. Gao, N. Guo, B. Gauvreau, M. Rajabian, O. Skorobogata, E. Pone, O. Zabeida, L. Martinu, C. Dubois, and M. Skorobogatiy, "Consecutive solvent evaporation and co-rolling techniques for polymer multilayer hollow fiber preform fabrication," vol. 21, 09 2006.

[20] C. J. Glassbrenner and G. A. Slack, "Thermal conductivity of silicon and germanium from 3°K to the melting point," *Phys. Rev.*, vol. 134, pp. A1058–A1069, May 1964. [Online]. Available: https://link.aps.org/doi/10.1103/PhysRev.134.A1058

[21] J. E. Graebner, "Thermal conductivity of diamond," in *Diamond: Electronic Properties and Applications*. Springer US, 1995, pp. 285–318. [Online]. Available: https://doi.org/10.1007/978-1-4615-2257-7_7

[22] M. Green, *Solar Cells: Operating Principles, Technology and System Applications*. Englewood Cliffs, NJ, Prentice-Hall, Inc., 1998.

[23] M. A. Green, "General temperature dependence of solar cell performance and implications for device modelling," *Progress in Photovoltaics: Research and Applications*, vol. 11, no. 5, pp. 333–340, 8 2003. [Online]. Available: http:https://doi.org/10.1002/pip.496

[24] M. A. Green, K. Emery, Y. Hishikawa, W. Warta, E. D. Dunlop, D. H. Levi, and A. W. Y. Ho-Baillie, "Solar cell efficiency tables (version 49)," *Progress in Photovoltaics: Research and Applications*, vol. 25, no. 1, pp. 3–13, 2017. [Online]. Available: http://dx.doi.org/10.1002/pip.2855

[25] J. P. Holman, *Heat transfer*, 8th ed. McGraw-Hill, 1997.

[26] F. Incropera, D. Dewitt, T. Bergman, A. Lavine, and S. Middleman, *Fundamentals of heat and mass transfer*, ser. Fundamentals of Heat and Mass Transfer. John Wiley, 2007, no. v. 1.

[27] L. Kehoe and G. M. Crean, "Thermal conductivity and specific heat determinations of a set of lead-free solder alloys," in *Proceedings. 4th International Symposium on Advanced Packaging Materials Processes, Properties and Interfaces (Cat. No.98EX153)*, Mar 1998, pp. 203–208.

[28] R. Kitamura, L. Pilon, and M. Jonasz, "Optical constants of silica glass from extreme ultraviolet to far infrared at near room temperature," *Applied optics*, vol. 46, no. 33, pp. 8118–8133, 2007.

[29] E. W. Lemmon and R. T. Jacobsen, "Viscosity and thermal conductivity equations for nitrogen, oxygen, argon, and air," *International Journal of Thermophysics*, vol. 25, no. 1, pp. 21–69, jan 2004. [Online]. Available: https://doi.org/10.1023/b:ijot.0000022327.04529.f3

[30] T. Luo, J. Garg, J. Shiomi, K. Esfarjani, and G. Chen, "Gallium arsenide thermal conductivity and optical phonon relaxation times from first-principles calculations," *EPL (Europhysics Letters)*, vol. 101, no. 1, p. 16001, 2013. [Online]. Available: http://stacks.iop.org/0295-5075/101/i=1/a=16001

[31] A. Luque and S. Hegedus, *Handbook of Photovoltaic Science and Engineering*. Wiley, 2011.

[32] L. Micheli, E. F. Fernández, F. Almonacid, T. K. Mallick, and G. P. Smestad, "Performance, limits and economic perspectives for passive cooling of high concentrator photovoltaics," *Solar Energy Materials and Solar Cells*, vol. 153, pp. 164 – 178, 2016. [Online]. Available: http://www.sciencedirect.com/science/article/pii/S0927024816300307

[33] "Reference solar spectral irradiance: Air mass 1.5," NREL. [Online]. Available: http://rredc.nrel.gov/solar/spectra/am1.5/

[34] "Reference solar spectral irradiance: Air mass zero," NREL. [Online]. Available: http://rredc.nrel.gov/solar/spectra/am0/

[35] N. Núñez, J. González, M. Vázquez, C. Algora, and P. Espinet, "Evaluation of the reliability of high concentrator gaas solar cells by means of temperature accelerated aging tests," *Progress in Photovoltaics: Research and Applications*, vol. 21, no. 5, pp. 1104–1113, 2013.

[36] P. Pérez-Higueras and E. Fernández, *High Concentrator Photovoltaics: Fundamentals, Engineering and Power Plants*, ser. Green Energy and Technology. Springer International Publishing, 2015.

[37] J. Piprek, *Semiconductor Optoelectronic Devices: Introduction to Physics and Simulation*, ser. Electronics & Electrical. Academic Press, 2003.

[38] M. L. Ramires, C. A. Nieto de Castro, Y. Nagasaka, A. Nagashima, M. J. Assael, and W. A. Wakeham, "Standard reference data for the thermal conductivity of water," *Journal of Physical and Chemical Reference Data*, vol. 24, no. 3, pp. 1377–1381, 1995.

[39] P. Rodrigo, L. Micheli, and F. Almonacid, *The High-Concentrator Photovoltaic Module*. Cham: Springer International Publishing, 2015, pp. 115–151. [Online]. Available: https://doi.org/10.1007/978-3-319-15039-0_5

[40] J. L. Sawin, F. Sverrisson, K. Seyboth, R. Adib, H. E. Murdock, C. Lins, I. Edwards, M. Hullin, L. H. Nguyen, S. S. Prillianto, K. Satzinger, F. Appavou, A. Brown, I. Chernyakhovskiy, J. Logan, M. Milligan, O. Zinaman, B. Epp, L. Huber, L. Lyons, T. Nowak, P. Otte, J. Skeen, B. Sovacool, B. Witkamp, E. Musolino, L. E. Williamson, L. Ashworth, and L. Mastny, "Renewables 2017 global status report," 2017.

[41] O. Z. Sharaf and M. F. Orhan, "Concentrated photovoltaic thermal (CPVT) solar collector systems: Part II – implemented systems, performance assessment, and future directions," *Renewable and Sustainable Energy*

Reviews, vol. 50, pp. 1566 – 1633, 2015. [Online]. Available: http://www.sciencedirect.com/science/article/pii/S1364032114006753

[42] W. Shockley and H. J. Queisser, "Detailed balance limit of efficiency of p-n junction solar cells," *Journal of applied physics*, vol. 32, no. 3, pp. 510–519, 1961.

[43] J. Speight, *Lange's Handbook of Chemistry, Seventeenth Edition*. McGraw-Hill Education, 2016.

[44] B. G. Streetman and S. Banerjee, *Solid state electronic devices*, 5th ed. Upper Saddle River, N.J. : Prentice Hall, 2000, includes bibliographical references and index.

[45] *Suncore's Concentrator Photovoltaic (CPV) Receiver*, Suncore Photovoltaic Technology Co., Ltd., 2015.

[46] M. Theristis and T. S. O'Donovan, "Electrical-thermal analysis of III–V triple-junction solar cells under variable spectra and ambient temperatures," *Solar Energy*, vol. 118, pp. 533 – 546, 2015. [Online]. Available: http://www.sciencedirect.com/science/article/pii/S0038092X15003059

[47] P. Tipler and R. Llewellyn, *Modern Physics*. W. H. Freeman, 2012.

[48] *Table of Emissivity of Various Surfaces*, TRANSMETRA haltec GmbH. [Online]. Available: http://www-eng.lbl.gov/~dw/projects/DW4229_LHC_detector_analysis/calculations/emissivity2.pdf

[49] R. C. Weast, "Handbook of chemistry and physics. 48th edition," *Physics Bulletin*, vol. 19, no. 3, p. 93, 1968. [Online]. Available: http://stacks.iop.org/0031-9112/19/i=3/a=027

[50] D. Widder, *The Heat Equation*, ser. Pure and Applied Mathematics. Elsevier Science, 1976.

[51] H. Zappe, *Introduction to Semiconductor Integrated Optics*, ser. Artech House optoelectronics library. Artech House, 1995.

[52] Z. Zhuang and F. Yu, "Optimization design of hybrid fresnel-based concentrator for generating uniformity irradiance with the broad solar spectrum," *Optics & Laser Technology*, vol. 60, pp. 27 – 33, 2014. [Online]. Available: http://www.sciencedirect.com/science/article/pii/S0030399213004799